이학박사학위논문

Intracellular Delivery of Plasmid DNA and Antiviral Peptides Using Nanoparticles and Cell-Penetrating Peptides

나노파티클과 세포 투과성 펩타이드를

이용한 플라스미드 유전자와 항바이러스성

펩타이드의 세포내 전달

2014 년 8 월

서울대학교 대학원

화학부 생화학전공

장 상 목

Intracellular Delivery of Plasmid DNA and Antiviral Peptides Using Nanoparticles and Cell-Penetrating Peptides

지도 교수 이 연

이 논문을 이학박사 학위논문으로 제출함

2014 년 7 월

서울대학교 대학원

화학부 생화학전공

장 상 목

장상목의 이학박사 학위논문을 인준함

2014 년 7 월

위 원 장 박 충 모 (인)

부위원장 이 연 (인)

위 원 박 종 상 (인)

위 원 유 재 훈 (인)

위 원 임 용 범 (인)

Intracellular Delivery of Plasmid DNA and Antiviral Peptides Using Nanoparticles and Cell-Penetrating Peptides

By Sangmok Jang

A Thesis Submitted to the Graduate Faculty of Seoul National University in Partial Fulfillment of the Requirement for the Degree of Doctor of Philosophy

July 2014

Abstract

The difficulty in delivering biomacromolecules such as nucleic acids, peptides, and proteins into cells through the cellular membranes warrants the need for the development of novel, potent delivery strategies. In particular, current non-viral strategies for delivering nucleic acids into cells using lipids and polymers present a significant hurdle to the success in pharmaceutical industry. Therefore, the development of safe and efficient nucleic acid delivery carriers has been proceeding rapidly. The CaP-based system is regarded as a reliable delivery system among the numerous delivery strategies being devised. However, the physiological instability and uncontrolled growth of CaP precipitates limit their application as efficient nucleic acid delivery carriers in biosystems. To overcome these barriers, I have synthesized a phosphate-based block copolymer, PEG-*b*-PMOEP (poly(ethylene glycol)-*b*-poly(2-methacryloyloxyethyl phosphate)), and have constructed calcium phosphate nanoparticles (CaPNs) coated with the block copolymer as an efficient and safe intracellular gene delivery carrier. While PEG block forms a shell to prevent uncontrolled growth of CaP precipitates, PMOEP block could be inserted into the calcium phosphate (CaP) core to entrap pDNA. The CaPNs showed no release of entrapped pDNA at physiological pH 7.4, but released pDNA at an endosomal pH 5.0 through a pH-dependent protonation of phosphate moieties. The PEG-*b*-PMOEP/CaP/pDNA nanoparticles exhibited great potential as gene delivery vehicles for future gene therapy applications.

The use of cell-penetrating peptides (CPPs) as a non-viral delivery vehicle requires the concentration of CPPs in the micromolar range, which is essential for CPPs to achieve a high cell-penetration ability. However, current technologies are associated with various disadvantages such as incomplete penetration of the peptides within a short time period and cell membrane damage due to the long-term exposure to the micromolar peptides. Therefore, I constructed monomeric LK-1 and LK-2 peptides, as well as dimeric α-helical cell-penetrating peptides (DHCPPs), named as LK-3 and LK-4, consisting of leucines (L) and lysines (K), by using a peptide stapling technique to enable the use of CPPs in the nanomolar range. The dimerization strategy based on a reducible disulfide bond or a non-reducible bond resulted in the high α-helical propensities of the peptides even in aqueous media. In particular, a strong correlation between α-helicity and cell-penetrating ability of the peptides was identified in the study. The LK peptides exhibited a strong binding affinity for the transactivation response element (TAR) RNA of human immunodeficiency virus-1 (HIV-1), as reported in the previous study. The TAR RNA of HIV-1 participates in the transcriptional elongation by interacting with the viral Tat protein. The LK dimers are able to efficiently penetrate the cell membrane for inhibiting the Tat-TAR interaction in mammalian cells without showing toxicity in the low concentration (i.e., nanomolar) range. The effective inhibition of HIV-1 replication in T-lymphoblastoid cells strongly suggests that the LK dimers have exhibited great potentials for use as antiviral peptides.

Keywords

Gene delivery, block copolymer, pH-sensitivity, Cell-Penenetrating Peptides (CPPs), HIV-1, peptide drug, Tat-TAR interaction, transcriptional inhibition

Student number : 2008-30098

Contents

Part II. Delivery of antiviral peptide drugs using dimeric α-helical cell-penetrating peptides with cell penetration activity

List of figures

Part I. Delivery of plasmid DNA using hybrid nanoparticles consisting of calcium phosphate and block copolymer with phosphomonoester moieties

Part II. Delivery of antiviral peptide drugs using dimeric α-helical cell-penetrating peptides with cell penetration activity

List of TABLES

Part I. Delivery of plasmid DNA using hybrid nanoparticles consisting of calcium phosphate and block copolymer with phosphomonoester moieties

Part II. Delivery of antiviral peptide drugs using dimeric α-helical cell penetrating peptides with cell penetration activity as well as antiviral activity

Part I. Delivery of plasmid DNA using hybrid nanoparticles consisting of calcium phosphate and block copolymer with phosphomonoester moieties

1. Abstract

I have synthesized a phosphate-based block copolymer, PEG-*b*-PMOEP (poly(ethylene glycol)-*b*-poly(2-methacryloyloxyethyl phosphate)), with a narrow molecular weight distribution (PD = 1.06) by atomic transfer radical polymerization (ATRP), and have constructed calcium phosphate nanoparticles (CaPNs) coated with the block copolymer as an efficient and safe intracellular gene delivery carrier. The phosphate-mimic PMOEP block could be incorporated into the calcium phosphate (CaP) core to entrap pDNA, with the PEG block forming a shell to prevent uncontrolled growth of CaP precipitates and aggregates in physiological fluids. The CaPNs showed high colloidal stability at pH 7.4, but released entrapped pDNA at an endosomal pH of 5.0 through a pH-dependent protonation of phosphate moieties for efficient endosomal escape. The PEG-*b*-PMOEP/CaP/pDNA nanoparticles, which were formed simply by mixing, exhibited great potential as gene delivery carriers for future gene therapy applications due to their high transfection efficiency, low toxicity, and good stability under physiological conditions.

2. Introduction

Calcium phosphate (CaP), the major component of bone, has been used as an important biomaterial for dental remodeling, tissue engineering, and drug delivery.[1-3] Due to the strong Coulombic interaction between calcium and phosphate ions that leads to hydration resistance, CaP has low aqueous solubility, an important characteristic for many of its applications. The addition of DNA to calcium and phosphate ions while forming CaP precipitates in aqueous solution allows the DNA to be incorporated as a co-precipitate. The CaP-DNA co-precipitate can be readily internalized into cells, and the entrapped DNA released into the cytosol, a phenomenon that has been recognized as an effective method for intracellular gene delivery since the 1960s.[4-5]

As the concept of gene therapy through delivery of nucleic acid drugs into cells has evolved as potential cures of human diseases, various non-viral gene delivery methods have been developed including polymer-DNA complexes (polyplex)[6-7], lipid-DNA complex (lipoplex)[8-9], and electroporation[10-11] due to the potential dangers of viral gene delivery methods.[12-13] Because the efficiency and safety of developed non-viral gene delivery methods for applications in human gene therapy are still unsatisfactory, only a small number of clinical trials have shown limited success.[14] Therefore, research into the development of efficient and safe gene delivery carriers is on-going, and the CaP co-precipitation method has been revived as an important and reliable delivery device candidate due to its efficiency, biocompatibility, bioresorbability, and

simple preparation. However, the uncontrolled growth and rapid decrease of physiological stability of CaP precipitates significantly limits their application as gene delivery carriers in biological systems. Large aggregates over several micrometers in diameter cannot be easily internalized into cells via the endocytic process[15], and can also block the blood stream in fine capillaries.[16-17] Additionally, the accumulation of large aggregates in organs such as the lungs, skin, or intestines can significantly reduce delivery efficiency and specificity.[16]

In order to control the growth and to improve the physiological stability of CaP precipitates with reproducible physicochemical characteristics that provide gene delivery with greater efficiency and safety, lipids and polymers have been used as detergents and coating materials. However, the process of preparing CaP micro- or nanoparticle emulsions in the presence of lipids[18] or polymers[19] requires relatively complex steps that include sonication or homogenization, which can damage DNA due to shearing forces. Alternatively, CaP nanoparticles can be efficiently prepared by the simple addition of a block copolymer during the co-precipitation process. If a block copolymer with a neutral hydrophilic block (e.g. poly(ethylene glycol) (PEG)) and a negatively charged block (e.g. poly(aspartic acid) (PAA)) is added to the calcium phosphate solution, the negatively charged block can be incorporated into the core of the CaP precipitate through interactions between the calcium ions and negatively charged moieties, and the neutral hydrophilic block can form a shell to prevent uncontrolled aggregation through steric repulsion.[20-23]

In this study, I synthesized PEG-*b*-PMOEP (poly(ethylene glycol)-*b*-poly(2-methacryloyloxyethyl phosphate)) with a narrow molecular weight distribution

(PD = 1.06) by atomic transfer radical polymerization (ATRP) (**Figure 1**), then prepared pDNA-encapsulated CaP nanoparticles (CaPNs) by coating with the PEG-*b*-PMOEP, and measured the enhancement of gene delivery efficiency with the nanocarrier. The PMOEP block, which resembles the head group of phosphatidic acid (PA), has many phosphomonoester moieties that strongly interact with calcium ions forming the CaP core, and the PEG block with a sufficient length (M_n = 5,000) forms a hydrophilic shell that can control the size of the CaP particle to approximately 200 nm. Phosphomonoester moieties have two distinct pK_a values, pK_{a1} =~3 and pK_{a1} =~7[24] unlike carboxylate moieties with pK_a of ~4. It was expected that doubly-charged phosphomonoester moieties could stabilize CaP nanoparticles at neutral pH via strong interaction with calcium ions, whereas the CaP nanoparticles could be destabilized by gradual protonation of the phosphomonoester moieties during the acidification in the early endosome allowing release of encapsulated nucleic acids. The enhancement of gene delivery efficiency by the phosphate-based polymer coating was analyzed by comparison with non-coated CaP precipitates and other gene delivery methods.

3. Materials and Method

3.1 Materials

Poly(ethylene glycol) mono-methyl ether (PEG-OH; M_n = 5,000, M_w = 5,300), 2-bromoisobutyryl bromide, triethylamine (TEA), 2-hydroxyethyl methacrylate (HEMA), dimethyl chlorophosphate (DCP), copper (I) bromide (CuBr), 2,2'-bipyridine (Bpy), trimethylsilyl bromide (TMSBr), calcium chloride ($CaCl_2$), 4-(2-hydroxyethyl)-1-piperazineethanesulfonic acid (HEPES), and 3-[4,5-dimethylthiazol-2-yl]-2,5-diphenyltetrazolium bromide (MTT) were purchased from Sigma-Aldrich (St. Louis, MO, USA). Methanol (MeOH), chloroform, and methylene chloride (MC) were purchased from Daejung (Siheung, Gyeonggi, Korea). The luciferase assay system and reporter lysis buffer were purchased from Promega (Madison, WI, USA). Dulbecco's Modified Eagle's Medium (DMEM), trypsin-EDTA, 100× antibiotic-antimycotic (penicillin, streptomycin, and amphotericin B), and fetal bovine serum (FBS) were purchased from GIBCO (Gaithersburg, MD, USA). Phosphate-buffered saline (PBS) was purchased from Cambrex Bio Science (Walkersville, MD, USA). All chemicals were used without further purification. The Micro BCA™ Protein Assay Kit was purchased from Pierce (Rockford, IL, USA). A firefly luciferase expression plasmid, pCN-Luci, was constructed by subcloning the cDNA of *Photinus pyralis* luciferase with the 21 amino acid nuclear localization signal of SV40 large T antigen into pCN plasmids. ExGen 500 was purchased from Fermentas (Burlington, Ontario, Canada).

3.2. Synthesis of PEG macroinitiator

PEG-OH (**1**) (2.0 g, 0.40 mmol) and TEA (390 μL, 2.8 mmol) were dissolved in 14mL of MC. After cooling the solution with an ice bath, 2-bromoisobutyrylbromide (**2**) (500 μL, 4.0 mmol) was slowly added to the vigorously stirred solution. The solution was further stirred at room temperature for 24 hr. The resulting PEG macroinitiator (**3**) could be purified by precipitation in diethyl ether (yield > 90%). The MALDI-TOF MS (Bruker Daltonics, Bremen, Germany) spectra of **1** and **3** are shown in **Figure 2**.

3.3. Synthesis of MPDME (2-methacryloyloxyethyl phosphoryldimethylester) monomer

HEMA (4.85 mL, 40.0 mmol) and pyridine (3.22 mL, 40.0 mmol) were dissolved in 15mL of chloroform. DCP (15.7 mL, 120 mmol) was added dropwise to the ice-cold solution under stirring. After stirring at room temperature for 48 h, the reaction mixture was diluted with chloroform (35 mL). The solution was then extracted with 100 mL of 0.1 *N* HCl, and the organic layer was collected, dried over $MgSO_4$, and concentrated by rotary evaporation to yield MPDME (**4**) (**Figure 3**).

^{1}H NMR (300 MHz, $CDCl_3$, δ ppm): δ1.93 (3H, CH_2=C***CH*****$_3$**CO_2-), δ3.80-4.00 (6H, -$(CH_2)_2$OPO(O***CH*****$_3$**$)_2$), δ4.20-4.50 (4H, -CO_2(***CH*****$_2$**$)_2$OPO-), δ5.90-6.10 (2H, ***CH*****$_2$**=CCH_3CO_2-)

3.4. Synthesis of PEG-*b*-PMPDME (PEG-*block*-poly(2-methacryloyloxyethyl phosphoryldimethylester))

PEG_{113}-*b*-$PMPDME_{50}$ (**5**) was synthesized by ATRP using **3** as a PEG_{113}-Br macroinitiator. **3** (0.20 g, 0.039 mmol) was added to a solution of MPDME (460 μL, 2.0 mmol) in MeOH (4mL). After three freeze-pump-thaw cycles, dried CuBr (12 mg, 0.078 mmol) and bpy (24 mg, 0.16 mmol) were added to the solution under an argon atmosphere. Polymerization was carried out at 40˚C for 12hr. After polymerization was complete, the solution was poured into excess ether to precipitate the product. **5** was obtained by drying the precipitate under vacuum (yield > 90%). The conversion efficiency from **3** was almost 99%. The ^{1}H NMR spectrum of **5** is shown in **Figure 4.** From the ^{1}H NMR spectrum, the degree of polymerization (DP) of PMPDME units was calculated to be 50.

3.5. Synthesis of PEG-*b*-PMOEP (PEG-*block*-poly(2-methacryloyloxyethyl phosphate))

PEG_{113}-*b*-$PMPDME_{50}$ (**5**) (190mg) was added to a solution of TMSBr (290 μL, 2.2 mmol) in MC (10mL) for deprotection of the phosphoesters.[25] After stirring at 0˚C for 20 h, the solution was poured into excess ether to precipitate the product. After drying the product under vacuum, it was dissolved in MC (5 mL), and the solution was dialyzed against MeOH, and then against deionized water (M.W.C.O. = 6,000-8,000). The final product (**6**) was obtained by lyophilization (yield > 95%). From the ^{1}H NMR spectrum (**Figure 5**), the degree of polymerization (DP) of PMOEP units was calculated to be 50. The molecular weight distribution of PEG_{113}-*b*-$PMOEP_{50}$ was determined by gel permeation chromatography (GPC) using a Superdex^{TM} 75 column (GE

healthcare, USA) calibrated by PEG standards. 50 mM Tris-HCl (pH 7.4) was used as the eluent at a flow rate of 0.7 mL/min at 35˚C.

3.6. PEG-*b*-PMOEP/CaP/pDNA nanoparticle preparation

A solution of 2.5 M $CaCl_2$ was added to a solution of pCN-Luci DNA in distilled water to prepare a 2× stock solution (Ca^{2+} 250mM, pCN-Luci DNA 10 μg/mL). An aliquot of the stock solution was quickly added to an equal volume of 2× PEG-*b*-PMOEP/phosphate solution (pH 7.1, 50 mM HEPES, 6.0 mM Na_2HPO_4, 300 mM NaCl). After vigorous mixing for a few seconds, the mixture was incubated at 47 ˚C for 24 h. The size distribution and zeta potential of nanoparticles in the suspension was analyzed at 37 ˚C by dynamic light scattering using a Zetasizer 3500 (Malvern Instruments, USA) equipped with a He-Ne ion laser at a wavelength of 633 nm.

3.7. Measurement of pCN-Luci DNA (pDNA) entrapment efficiency

After the formation of PEG-*b*-PMOEP/CaP/pDNA nanoparticles, the sample suspension was centrifuged at 15,000×g for 30 min to precipitate the nanoparticles. The pDNA concentration in the supernatant was calculated from the absorbance at 260 nm. Entrapment efficiency (%EE) was determined using the following equation:

$$\%\mathrm{EE} = \frac{[A]_0 - [A]_s}{[A]_0} \times 100$$

where $[A]_0$ and $[A]_s$ are the OD values of the initial pDNA solution and the supernatant, respectively.

3.8. pH-sensitive release of pDNA

The PEG-*b*-PMOEP/CaP/pDNA nanoparticle solution (PEG-*b*-PMOEP concentration = 500 μg/mL) was centrifuged at 13,000×g for 10 min. The supernatant was carefully removed, and the precipitate was resuspended in two aqueous buffer solutions (pH 7.4 and pH 5.0). Each sample was dialyzed against buffer solution at 37 ˚C using a D-Tube dialyzer (M.W.C.O. = 6,000-8,000). Agarose gel electrophoresis on 1.0% (w/v) agarose gel was used for analysis of DNA release. After electrophoresis, the gel was stained with ethidium bromide solution (0.5 μg/mL), and the DNA band was visualized on a UV illuminator. The intensity of the DNA band was analyzed by a gel image analysis software (GelQuant.NET software, Biochemlabsolutions.com).

3.9. Cytotoxicity assay

To determine the cytotoxicity of the nanoparticles, MTT assays were performed. HeLa cells were seeded in 96-well tissue culture dishes at 5,000 cells/well in 90 μL of DMEM containing 10% FBS for 24 h before transfection. After replacing the medium with fresh complete medium, 30 μL of each sample was added and the cells were further incubated for 24 h. 20 μL of filtered MTT solution (2 mg/mL in PBS) was added to each well. After incubation for 4 h at 37˚C, the medium was removed from the wells and 150 μL of DMSO was added to dissolve the formazan crystals. Absorbance was measured at 570 nm using a microplate reader (Molecular Devices Co., Menlo Park, CA, USA) and cell viability was calculated by comparison with untreated control cells. Triplicate experiments were performed for determining the average value and

standard deviation.

3.10. Statistical analysis

All statistical analysis was performed using a t-test between individual treatment groups, using the Graphpad Prism 6.0 software (GraphPad software Inc.).

3.11. Transfection and luciferase assay

HeLa cells (human cervical cancer cells) were grown in complete medium (DMEM supplemented with 10% FBS and 1% antibiotics) at 37 ˚C in a humidified 5% CO_2 incubator. HeLa cells were seeded at a density of 15,000 cells/well into 24-well tissue culture dishes in 600 μL of complete medium for 24 h before transfection. 120 μL of all samples (pDNA only, CaP normal, CaPNs, ExGen 500) with complete medium (DMEM supplemented with 10% FBS and 1% antibiotics) were added to the cells at a final pCN-Luci DNA concentration of 0.5~4 μg/mL and the cells were further incubated for 48 h.

For the transfection with ExGen 500, N/P ratio of 6 was used as an optimal transfection condition. For the luciferase assay, the growth medium was removed and the cells were washed with PBS and lysed for 30 min at room temperature with 150 μL of reporter lysis buffer. Luciferase activity in the transfected cells was measured using an LB 9507 luminometer (Berthold, Germany) with 10 μL of the lysate dispensed into a luminometer tube and the automatic injection of 50 μL of Luciferase Assay Reagent. The protein concentration of the lysate was determined using a Micro™ BCA protein assay

kit. Luciferase activity was measured in terms of relative light units (RLU) and the final values were determined as RLU/mg of total protein in the lysate. Triplicate experiments were performed for determining the average value and standard deviation.

4. Results and discussion

4.1. Synthesis of PEG-*b*-PMOEP

ATRP is one of the most powerful methods to control the polymerization of a wide range of monomers.[26] In this study, a diblock copolymer with a neutral hydrophilic PEG block and a negatively charged phosphate block, PEG-*b*-PMOEP (**6**), was synthesized by ATRP to form a surface coating for CaP nanoparticles (CaPNs). The PEG macroinitiator, PEG-Br (**3**), was synthesized from PEG-OH (**1**) and 2-bromoisobutyryl bromide (**2**). Because it was difficult to determine the conjugation efficiency by ^{1}H-NMR due to the relatively small number of terminal residues, MALDI-TOF was used as an alternative method to compare the molecular weight difference between **1** and **3**. **Figure 2** shows that the conversion from **1** to **3** was almost 100% efficient. The phosphoryldimethylester monomer, MPDME (**4**), was prepared from HEMA and DCP since ATRP is often hampered by the presence of acid groups.[27-28] In addition, MPDME (**4**) was quite soluble in alcoholic ATRP solvents that were used to dissolve the PEG macroinitiator.

PEG-*b*-PMPDME (**5**) was synthesized from the PEG macroinitiator (**3**) using CuBr and bpy as the catalyst and ligand, respectively (Figure 3 (a)). PEG-*b*-PMOEP (**6**) was easily obtained through demethylation of **5**. After demethylation, proton peaks at δ3.80-4.00 ppm corresponding to dimethyl esters of **5** had completely disappeared from the ^{1}H-NMR spectrum (**Figure 5**). The molecular weight distribution of the product block polymer was analyzed by both ^{1}H-NMR and GPC (**Table 1**). From ^{1}H-NMR, the degree of

polymerization (DP) of the PMOEP block was calculated to be 50. The polydispersity (PD) of **6** was 1.06, which represents a successful ATRP polymerization of the phosphate-based block copolymer with a narrow molecular weight distribution.

4.2. Preparation of PEG-*b*-PMOEP/CaP/pDNA nanoparticles

The newly synthesized phosphate-based block copolymer, PEG-*b*-PMOEP, was used to prepare pDNA-encapsulated CaPNs for gene delivery. When calcium ions were mixed with phosphate ions, mixed salts including monocalcium phosphate ($Ca(H_2PO_4)_2$) and dicalcium phosphate ($CaHPO_4$) were formed depending on the pH of the solution. DNA could be readily incorporated into the CaP precipitates during the precipitation process. Growth of the precipitates was difficult to be controlled and very heterogeneous precipitates were formed without stabilizing reagents. In presence of PEG-*b*-PMOEP, the phosphate-based PMOEP block could be incorporated into the CaP precipitate core, and the neutral hydrophilic PEG block could coat the surface of the CaP. Because a PEG of short length is not sufficient for complete shielding and steric stabilization of nanoparticles to prevent protein-nanoparticle interactions in physiological fluids[29], I chose the PEG block with M_n = 5,000 for stabilization of CaP particles.

pDNA-encapsulated CaP nanoparticles were simply prepared by mixing Ca^{2+}/pDNA and phosphate/PEG-*b*-PMOEP solutions. The colloidal stability of CaPNs was highly dependent upon the concentration of the phosphate based block copolymer. CaPNs less than 200 nm in diameter formed only with

concentrations of the block copolymer over 380 μg/mL (**Figure 6**). In the range of 400 μg/mL to 500 μg/mL, PEG-*b*-PMOEP/CaP/pDNA nanoparticles of approximately 180 nm in size were obtained. These CaPNs showed a unimodal size distribution with polydispersity indices (PDI) ranging from 0.1 to 0.2, which was confirmed by dynamic light scattering (DLS) analysis (**Figure 7-8**). The incubation temperature was another important factor for successful formation of PEG-*b*-PMOEP/CaP/pDNA nanoparticles. CaPNs with narrower size distributions were generally obtained as the temperature was increased (data not shown). Considering both narrow size distributions and thermal denaturation of pDNA at higher temperatures, I determined the optimal temperature to be 47 ℃ for the transfection experiments shown below.

4.3. Measurement of pDNA entrapment efficiency and zeta potential from PEG-*b*-PMOEP/CaP/pDNA nanoparticles

The entrapment efficiency of pDNA in the polymer-coated CaPNs was measured by UV absorbance at 260 nm. **Figure 9** shows the entrapment efficiency and zeta potential for three different PEG-*b*-PMOEP concentrations (0, 440, and 500 μg/mL). All samples had showed that more than 80% of the pDNA loaded into the CaP particles, which suggests that the pDNA incorporation efficiency was not closely related with the polymer coating but was affected by the co-precipitation process. However, the surface charges of CaP particles were strongly dependent upon the polymer coating. CaP normal showed a zeta potential of about +33 mV, but polymer-coated CaPNs showed a zeta potential closed to zero, which suggested that neutral hydrophilic PEG

block formed a shell on the surface of CaPNs.

4.4. pH-sensitive release of pDNA from PEG-*b*-PMOEP/CaP/pDNA nanoparticles

Because the electrostatic interaction between Ca^{2+} and $H_2PO_4^-$ is weaker than between Ca^{2+} and HPO_4^{2-}, the aqueous solubility of CaP increases as the pH decreases.[30] It was also expected that the interaction between PEG-*b*-PMOEP and Ca^{2+} would decrease as a result of gradual protonation of phosphate groups in the PMOEP backbone.

Nanoparticles of several hundred nanometers in size are readily internalized into cells through the endocytic process, an important pathway for efficient intracellular drug/gene delivery.[31] Subsequently, internalized nanoparticles should escape the endosome into the cytosol before full acidification (pH 4) or maturation to a lysosome in which degrading enzymes are activated.[32] It was expected that the dissolution of CaP into calcium and phosphate ions at acidic pH can increase osmotic pressure in the endosome to induce endosomal membrane rupture by osmotic swelling and released pDNA from CaP can escape the endosome efficiently.[33]

Therefore, release of pDNA from CaPNs at the endosomal pH 5.0 and normal physiological pH 7.4 were compared. **Figure 10** shows the result of agarose gel electrophoresis after incubation of PEG-*b*-PMOEP/CaP/pDNA nanoparticles at the two different pH values. At pH 7.4, no release of pDNA from the nanoparticles was detected even after 24 h and the nanoparticles maintained a narrow size distribution with high colloidal stability even after 72 h (data not

shown). On the other hand, pDNA release began after 1 h at pH 5.0 with about 70% of the pDNA released from the CaPNs after 1 h and almost 95% released after 2 h as measured by a gel image analysis software (**Figure 11**). These results strongly support the supposition that PEG-*b*-PMOEP/CaP/pDNA nanoparticles can dissociate and the released pDNA can escape the endosome in the weakly acidic early endosomal state before degradation and inactivation of pDNA in the lysosome.

4.5. Cytotoxicity assay of HeLa cells by PEG-*b*-PMOEP and PEG-*b*-PMOEP/CaP/pDNA nanoparticles

Cytotoxicity of free PEG-*b*-PMOEP and CaPNs was measured separately by the MTT assay. Compared to ExGen 500 (linear polyethylenimine), a commercially available transfection reagent, which showed about 20% of cell viability at the concentration of 10 μg/mL, free PEG-*b*-PMOEP showed almost no cytotoxicity even at the polymer concentration of 40 μg/mL (**Figure 12**). Additionally, non-toxicity of PEG-*b*-PMOEP/CaP/pDNA nanoparticles (CaPN 2) was also confirmed until the pDNA concentration of 4 μg/mL (**Figure 13**). The cytotoxicity results support the potential of PEG-*b*-PMOEP/CaP/pDNA nanoparticles as safe gene delivery carriers for use in biosystems.

4.6. Confocal Laser Scanning Microscopy (CLSM) observation of HeLa cells by cy5-labeled pDNA

As shown in confocal laser scanning miscroscopy (CLSM) images (**Figure 14-15**), normal CaP precipitates were difficult to be internalized into HeLa cells

in spite of their positive surface charges, the PEG-*b*-PMOEP-coated CaPNs with almost neutral surface charges were efficiently internalized by endocytic pathways.

4.7. Transfection of HeLa cells and luciferase assay by PEG-*b*-PMOEP/CaP/pDNA nanoparticles

Transfection experiments of HeLa cells were performed with PEG-*b*-PMOEP/CaP/pDNA nanoparticles. As shown in **Figure 16**, the PEG-*b*-PMOEP-coated CaPNs showed about 2-fold higher transfection efficiency than normal CaP precipitates. By controlling the size of CaP precipitates to approximately 200 nm, the transfection efficiency could be significantly enhanced, probably due to more effective endocytic uptake of CaPNs compared to simple heterogeneous CaP precipitates with an average size over several micrometers.[19]

The effect of the initial PEG-*b*-PMOEP concentrations on transfection efficiency was negligible. For comparison with other non-viral gene delivery carriers, ExGen 500 was used as a positive control. Our CaPNs showed higher transfection efficiency compared to ExGen 500 at the pDNA concentration range of 0.5~4 μg/mL (**Figure 17**). The transfection efficiency of CaPNs and ExGen 500 polyplexes were gradually increased as the pDNA concentration was increased. It is probably due to increased uptake of CaPNs at higher pDNA concentrations.

Cationic polymer-pDNA complexes such as *b*-PEI-pDNA complex generally show high *in vitro* transfection efficiency due to their positive surface charges,

however, they are difficult to apply to *in vivo* gene delivery due to the formation of large aggregates with negatively charged serum proteins.[34] Surface coating of the complexes with biocompatible hydrophilic polymers might be required to prevent such aggregation, but transfection efficiency is often reduced with a polymer coating.[35] Considering that the transfection efficiency of our PEG-*b*-PMOEP/CaP/pDNA nanoparticles was higher than that of the ExGen 500-pDNA complex even in the presence of a PEG shell, the CaPNs have great potential as *in vivo* gene delivery carriers with both high delivery efficiency and safety.

5. Conclusion

PEG-*b*-PMOEP coated CaP nanoparticles were prepared as carriers for the efficient intracellular delivery of pDNA. The phosphate-based block copolymer strongly interacts with calcium ions and prevents the uncontrolled growth of CaP precipitates. Simple addition of the phosphate-based polymer led to CaP nanoparticles being formed with an average size below 200nm, a narrow size distribution, high pDNA entrapment efficiency, good colloidal stability at neutral pH, and allowed the selective release of the pDNA at weakly acidic pH. Compared to the uncoated CaP precipitate and ExGen 500, the PEG-*b*-PMOEP coated CaP nanoparticles exhibited great potential as efficient and safe gene delivery carriers for future gene therapy applications.

6. References

1. Peter, B. et al. Calcium phosphate drug delivery system: influence of local zoledronate release on bone implant osteointegration. *Bone* **36**, 52-60 (2005).

2. Xie, C., Lu, H., Li, W., Chen, F.M. & Zhao, Y.M. The use of calcium phosphate-based biomaterials in implant dentistry. *Journal of Materials Science-Materials in Medicine* **23**, 853-862 (2012).

3. Rosa, V., Della Bona, A., Cavalcanti, B.N. & Nor, J.E. Tissue engineering: From research to dental clinics. *Dental Materials* **28**, 341-348 (2012).

4. Liu, T. et al. Calcium phosphate nanoparticles as a novel nonviral vector for efficient trasfection of DNA in cancer gene therapy. *Cancer Biotherapy and Radiopharmaceuticals* **20**, 141-149 (2005).

5. Tabaković, A., Kester, M. & Adair, J.H. Calcium phosphate-based composite nanoparticles in bioimaging and therapeutic delivery applications. *Wiley Interdisciplinary Reviews: Nanomedicine and Nanobiotechnology* **4**, 96-112 (2012).

6. Boussif, O. et al. A versatile vector for gene and oligonucleotide transfer into cells in culture and in vivo: polyethylenimine. *Proceedings of the National Academy of Sciences* **92**, 7297-7301 (1995).

7. Lee, Y. et al. Charge-conversion ternary polyplex with endosome disruption moiety: A technique for efficient and safe gene delivery. *Angewandte Chemie-International Edition* **47**, 5163-5166 (2008).

8. Zhou, X. & Huang, L. DNA transfection mediated by cationic liposomes containing lipopolylysine: characterization and mechanism of action.

Biochimica et Biophysica Acta (BBA) - Biomembranes **1189**, 195-203 (1994).

9. Ewert, K. et al. Cationic lipid-DNA complexes for gene therapy: Understanding the relationship between complex structure and gene delivery pathways at the molecular level. *Current Medicinal Chemistry* **11**, 133-149 (2004).

10. Paquereau, L. & Le Cam, A. Electroporation-mediated gene transfer into hepatocytes: Preservation of a growth hormone response. *Analytical Biochemistry* **204**, 147-151 (1992).

11. Jaroszeski, M.J., Gilbert, R., Nicolau, C. & Heller, R. In vivo gene delivery by electroporation. *Advanced Drug Delivery Reviews* **35**, 131-137 (1999).

12. Marshall, E. Gene Therapy Death Prompts Review of Adenovirus Vector. *Science* **286**, 2244-2245 (1999).

13. Kaiser, J. Seeking the Cause of Induced Leukemias in X-SCID Trial. *Science* **299**, 495 (2003).

14. Kwon, M.J. et al. Effective healing of diabetic skin wounds by using nonviral gene therapy based on minicircle vascular endothelial growth factor DNA and a cationic dendrimer. *The Journal of Gene Medicine* **14**, 272-278 (2012).

15. Zhang, S.L., Li, J., Lykotrafitis, G., Bao, G. & Suresh, S. Size-Dependent Endocytosis of Nanoparticles. *Advanced Materials* **21**, 419-424 (2009).

16. Lee, Y. & Kataoka, K. Delivery of Nucleic Acid Drugs. *Advanced Polymer Science* **249**, 95-134 (2012).

17. Minireview: Delivering the Code: Polyplex Carriers for Deoxyribonucleic Acid and Ribonucleic Acid Interference Therapies. *Endocrinology* **151**, 466-

473 (2010).

18. Yang, Y., Li, J., Liu, F. & Huang, L. Systemic Delivery of siRNA via LCP Nanoparticle Efficiently Inhibits Lung Metastasis. *Molecular Therapy* **20**, 609-615 (2012).

19. Roy, I., Mitra, S., Maitra, A. & Mozumdar, S. Calcium phosphate nanoparticles as novel non-viral vectors for targeted gene delivery. *International Journal of Pharmaceutics* **250**, 25-33 (2003).

20. Kakizawa, Y. & Kataoka, K. Block copolymer self-assembly into monodispersive nanoparticles with hybrid core of antisense DNA and calcium phosphate. *Langmuir* **18**, 4539-4543 (2002).

21. Kakizawa, Y., Furukawa, S. & Kataoka, K. Block copolymer-coated calcium phosphate nanoparticles sensing intracellular environment for oligodeoxynucleotide and siRNA delivery. *Journal of Controlled Release* **97**, 345-356 (2004).

22. Kakizawa, Y., Furukawa, S., Ishii, A. & Kataoka, K. Organic-inorganic hybrid-nanocarrier of siRNA constructing through the self-assembly of calcium phosphate and PEG-based block aniomer. *Journal of Controlled Release* **111**, 368-370 (2006).

23. Pittella, F. et al. Enhanced endosomal escape of siRNA-incorporating hybrid nanoparticles from calcium phosphate and PEG-block charge-conversional polymer for efficient gene knockdown with negligible cytotoxicity. *Biomaterials* **32**, 3106-3114 (2011).

24. Kooijman, E.E. et al. What Makes the Bioactive Lipids Phosphatidic Acid and Lysophosphatidic Acid So Special? *Biochemistry* **44**, 17007-17015 (2005).

25. Sparrow, J.T. & Monera, O.D. Improvements to the TMSBr method of peptide resin deprotection and cleavage: Application to large peptides. *Peptide Research* **9**, 218-222 (1996).

26. Sant, V.P., Smith, D. & Leroux, J.-C. Novel pH-sensitive supramolecular assemblies for oral delivery of poorly water soluble drugs: preparation and characterization. *Journal of Controlled Release* **97**, 301-312 (2004).

27. Zhou, F. & Huck, W.T.S. Three-stage switching of surface wetting using phosphate-bearing polymer brushes. *Chemical Communications* **48**, 5999-6001 (2005).

28. Suzuki, S., Whittaker, M.R., Grøndahl, L., Monteiro, M.J. & Wentrup-Byrne, E. Synthesis of Soluble Phosphate Polymers by RAFT and Their in Vitro Mineralization. *Biomacromolecules* **7**, 3178-3187 (2006).

29. Wang, G. & Uludag, H. Recent developments in nanoparticle-based drug delivery and targeting systems with emphasis on protein-based nanoparticles. *Expert Opinion on Drug Delivery* **5**, 499-515 (2008).

30. Dorozhkin, S.V. Dissolution mechanism of calcium apatites in acids: A review of literature. *World Journal of Methodology* **2**, 1-17 (2012).

31. Khalil, I.A., Kogure, K., Akita, H. & Harashima, H. Uptake pathways and subsequent intracellular trafficking in nonviral gene delivery. *Pharmacological Reviews* **58**, 32-45 (2006).

32. Breunig, M., Bauer, S. & Goefferich, A. Polymers and nanoparticles: Intelligent tools for intracellular targeting? *European Journal of Pharmaceutics and Biopharmaceutics* **68**, 112-128 (2008).

33. Bisht, S., Bhakta, G., Mitra, S. & Maitra, A. pDNA loaded calcium

phosphate nanoparticles: highly efficient non-viral vector for gene delivery. *International Journal of Pharmaceutics* **288**, 157-168 (2005).

34. van Gaal, E.V.B. et al. How to screen non-viral gene delivery systems in vitro? *Journal of Controlled Release* **154**, 218-232 (2011).

35. Papanicolaou, I., Briggs, S. & Alpar, H.O. Increased Resistance of DNA Lipoplexes to Protein Binding In Vitro by Surface-modification with a Multivalent Hydrophilic Polymer. *Journal of Drug Targeting* **12**, 541-547 (2004).

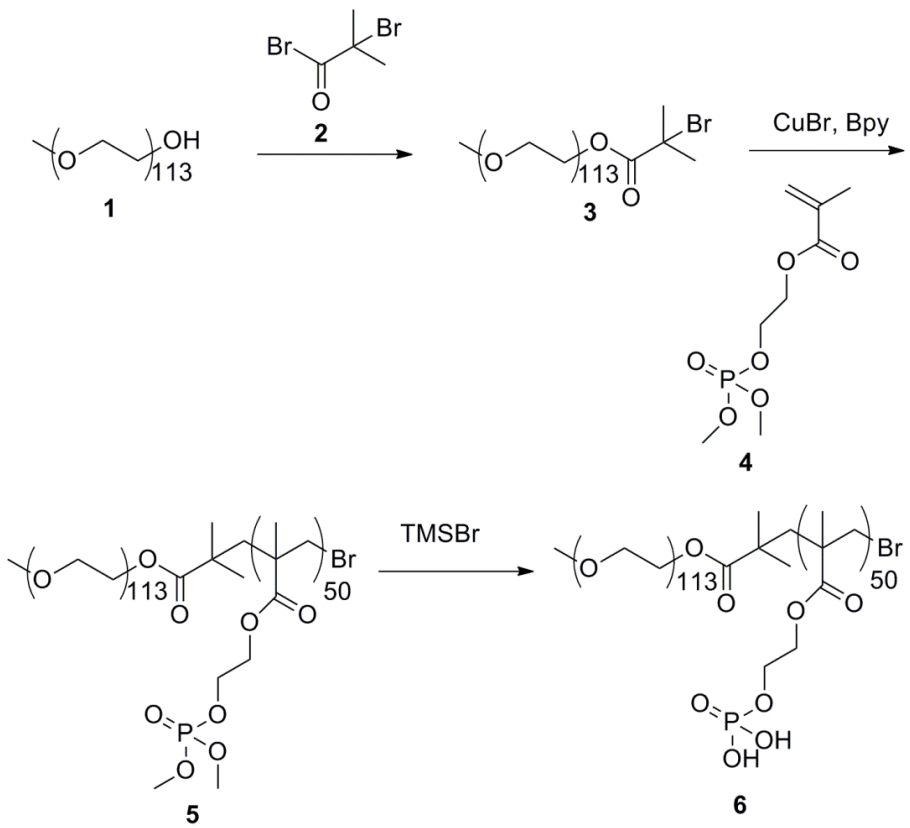

Figure 1. Synthetic scheme of PEG-*b*-PMOEP (**6**) by ATRP

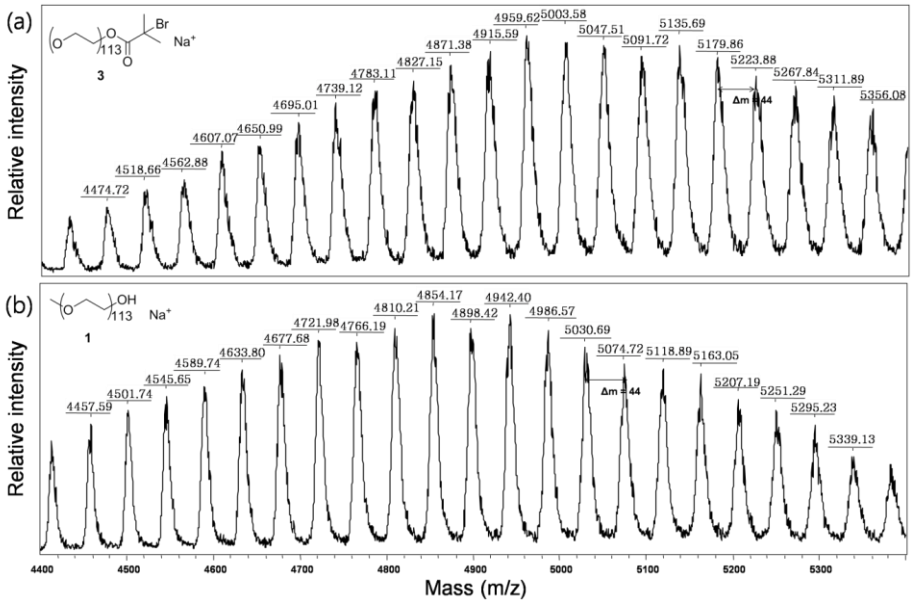

Figure 2. Maldi-TOF mass spectra of PEG (**1**) and PEG macroinitiator (**3**)

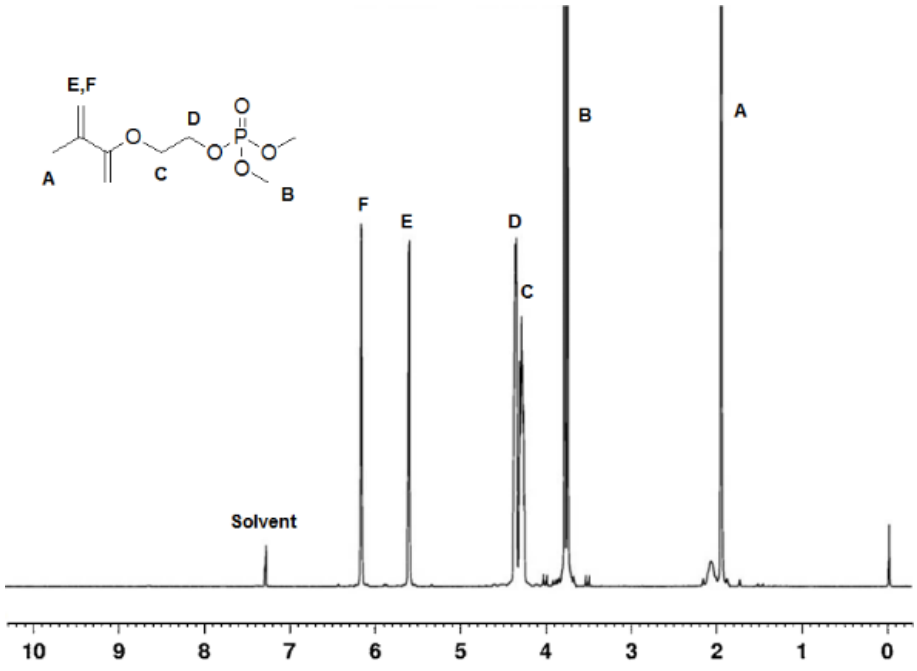

Figure 3. ^{1}H NMR spectra of MOEP monomer (**4**) in $CDCl_3$

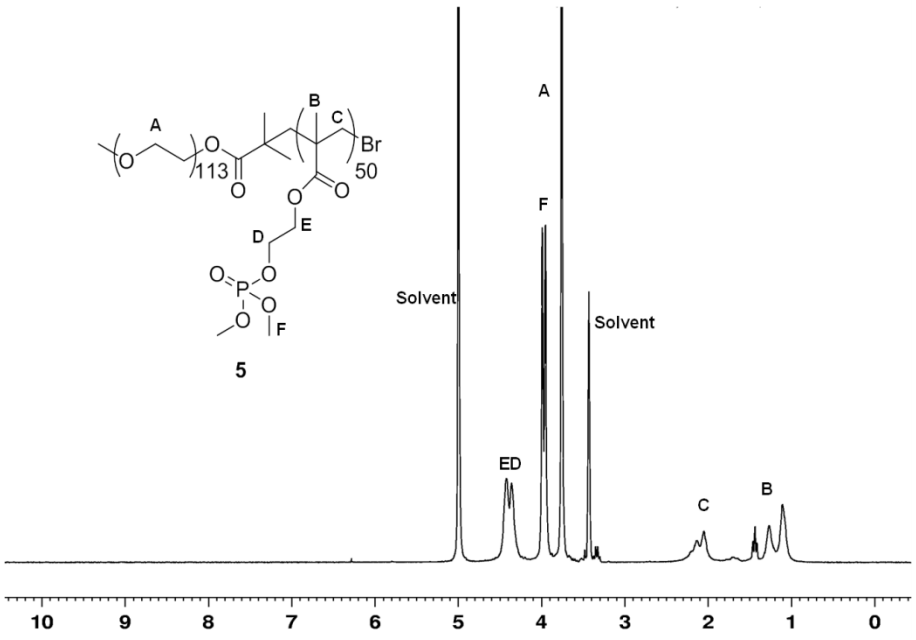

Figure 4. ^{1}H NMR spectra of PEG-*b*-PMPDME (**5**) in CD_3OD

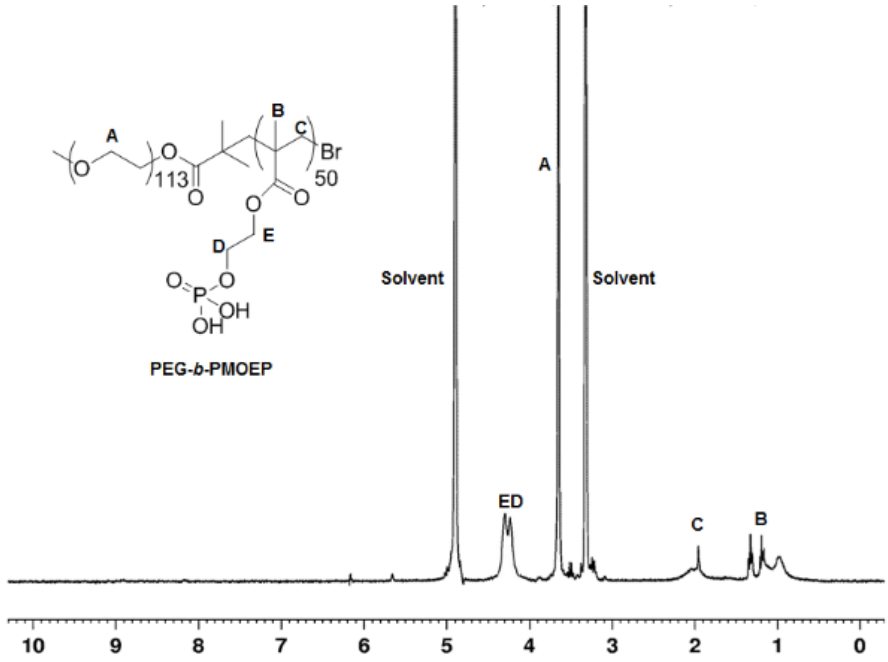

Figure 5. ^{1}H NMR spectra of PEG-*b*-PMOEP (**6**) in CD_3OD

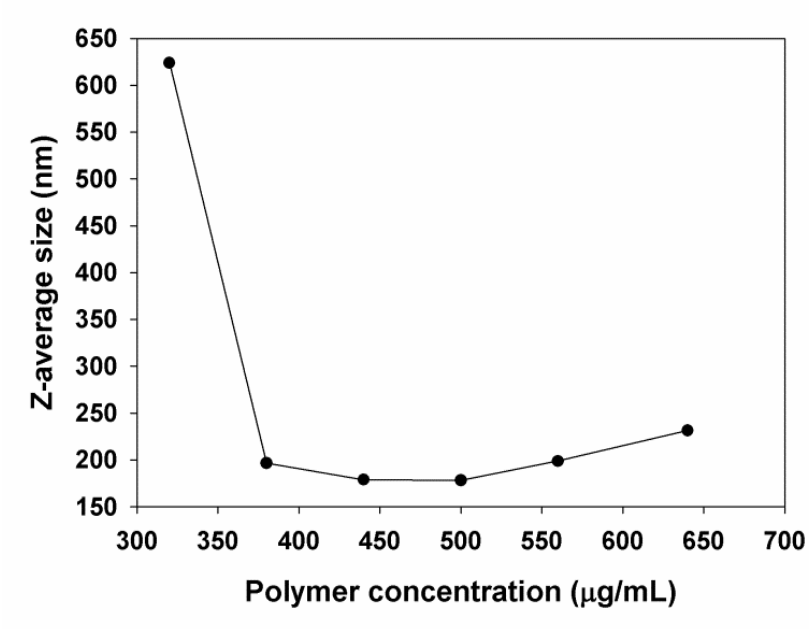

Figure 6. Polymer concentration dependence of the size of the PEG-*b*-PMOEP coated CaP nanoparticles.

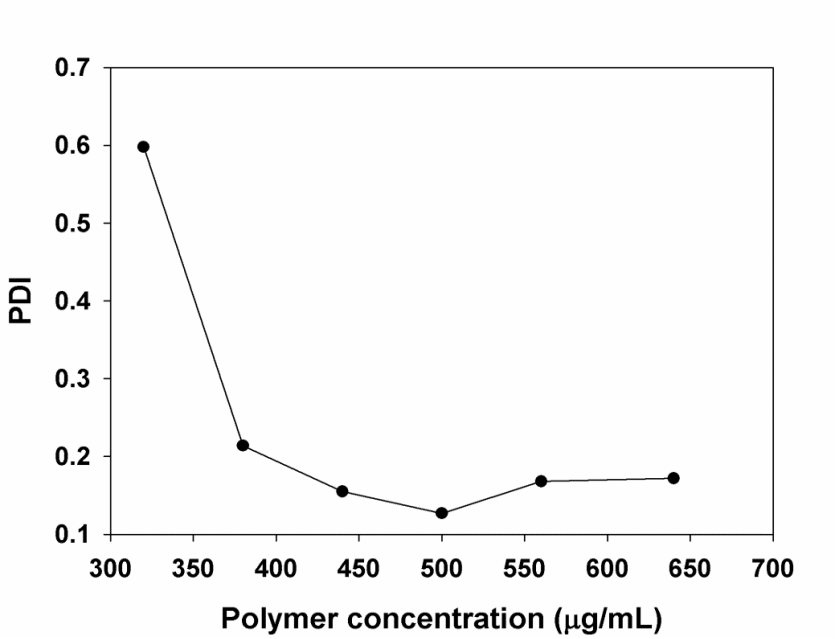

Figure 7. Polymer concentration dependence of the PDI of the PEG-*b*-PMOEP coated CaP nanoparticles.

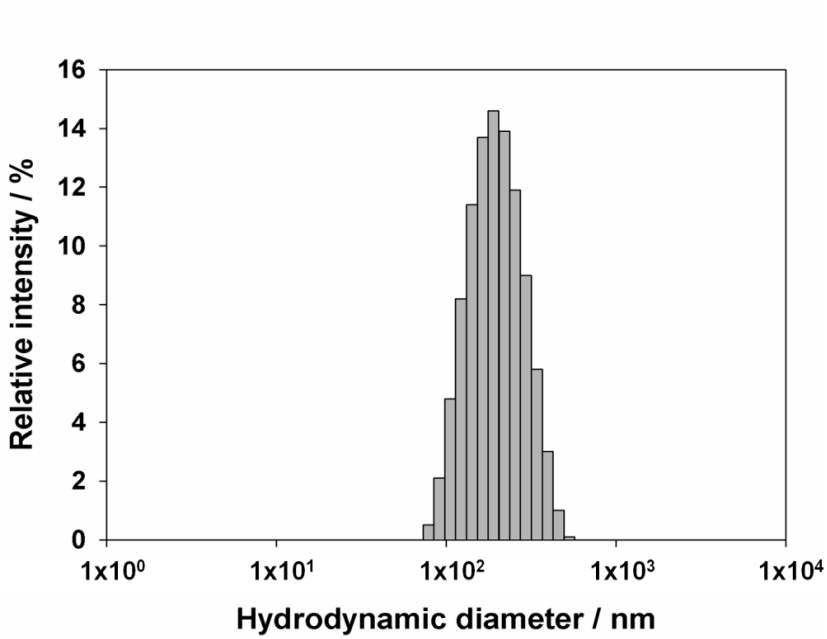

Figure 8. The sized distribution of the CaP nanoparticles (PEG-*b*-PMOEP concentration = 500 μg/mL).

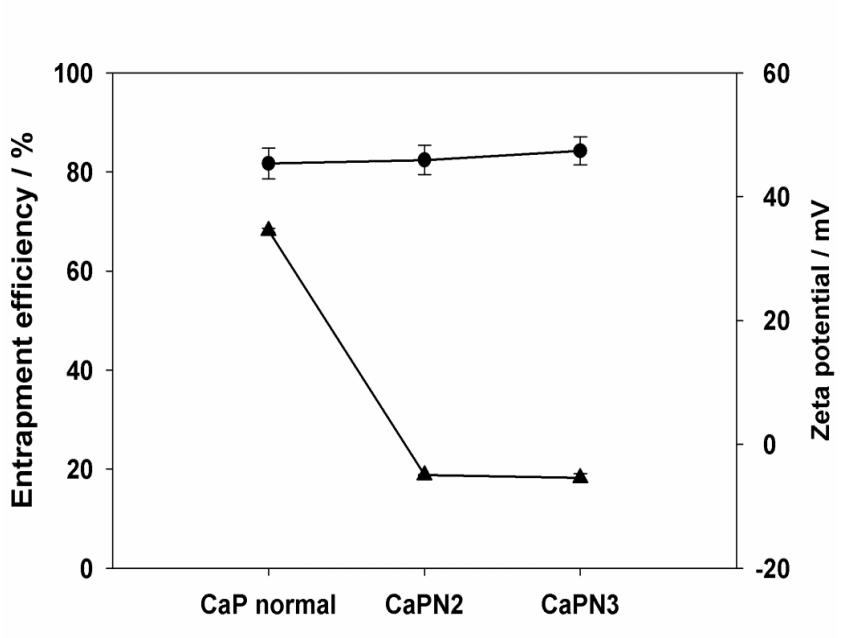

Figure 9. Entrapment efficiency of pDNA loaded PEG-*b*-PMOEP/CaP nanoparticles (PEG-*b*-PMOEP concentration of CaPN 1, CaPN 2, CaPN 3 = 0, 440, 500 μg/mL, respectively). Each error bar represents the standard deviation (n = 3).

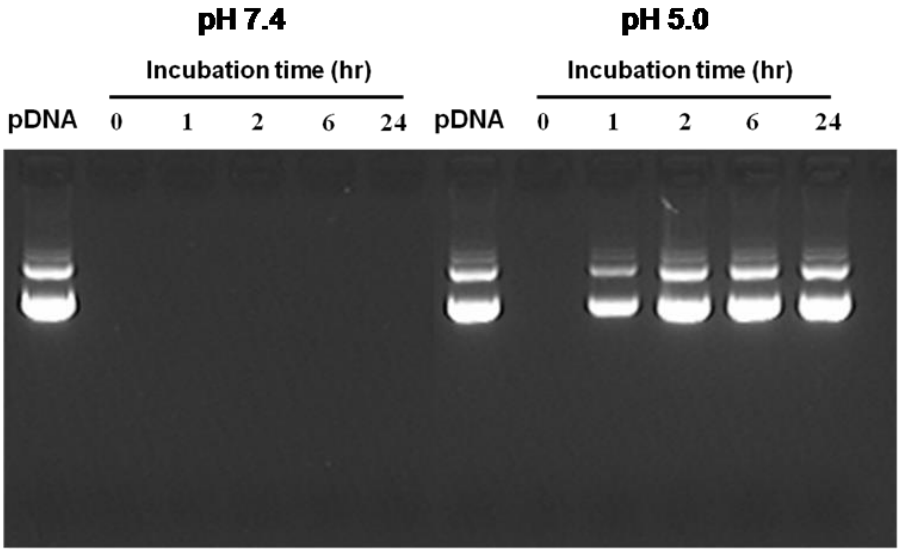

Figure 10. pH-sensitive release of pDNA from PEG-*b*-PMOEP/CaP nanoparticles according to the incubation time on pH 7.4 and pH 5.0, respectively.

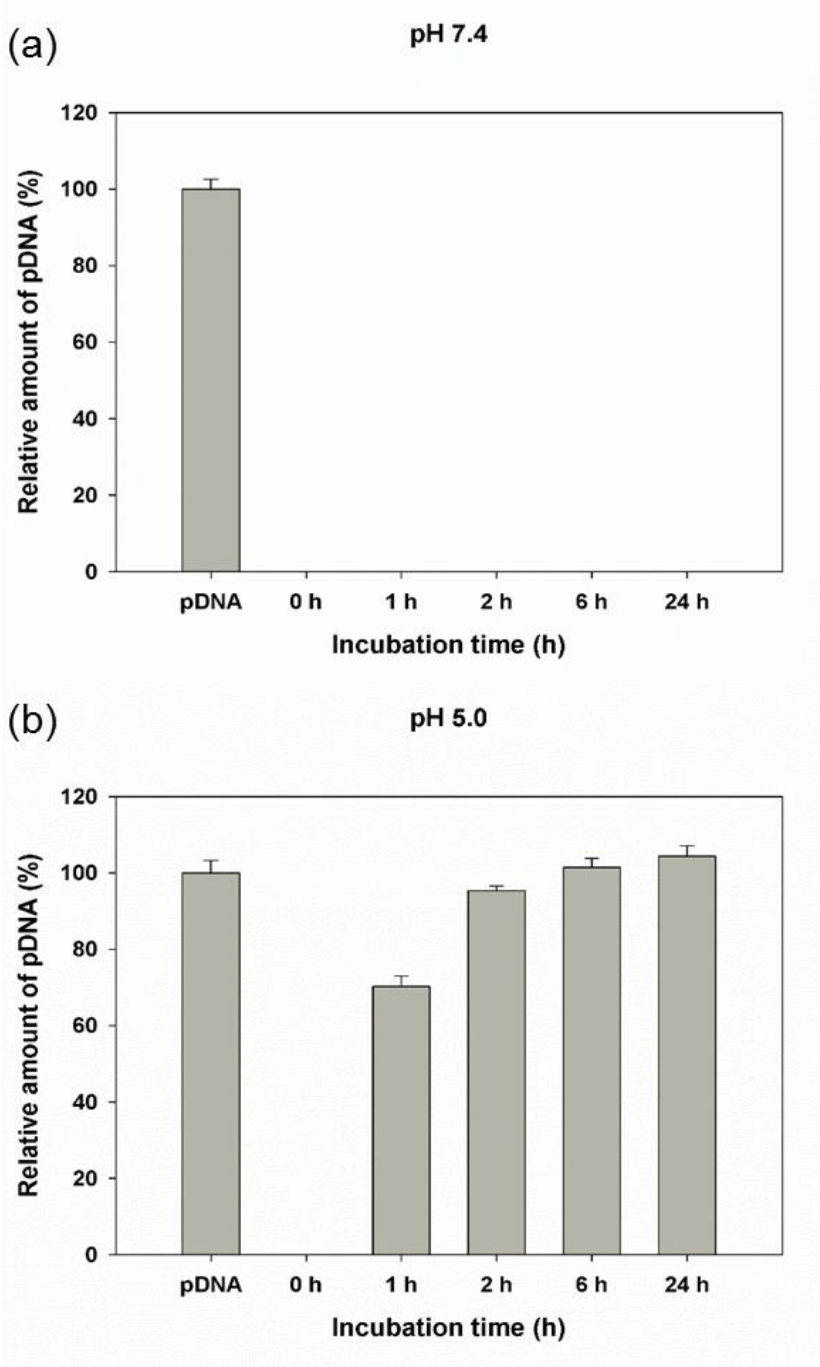

Figure 11. Relative amount of pDNA from PEG-*b*-PMOEP/CaP nanoparticles according to the incubation time on (a) pH 7.4 and (b) pH 5.0, respectively. Each error bar represents the standard deviation (n = 3).

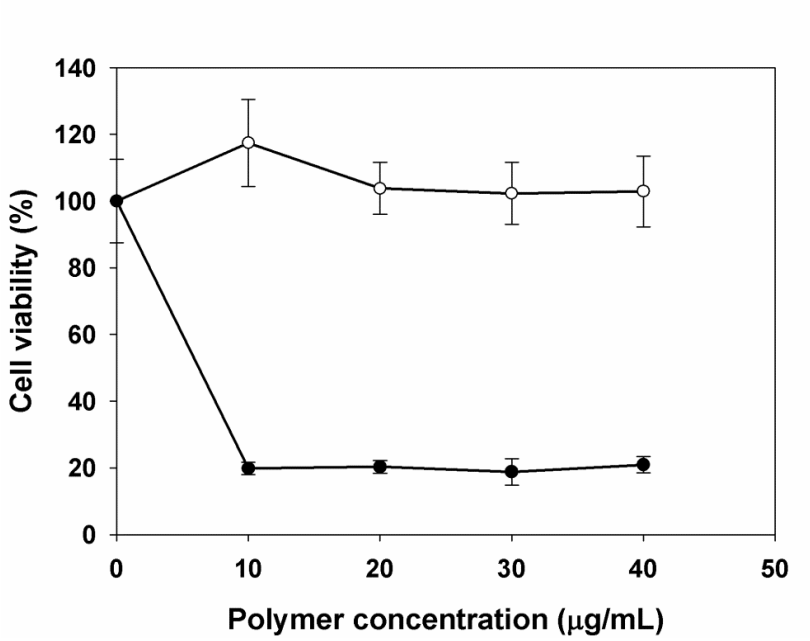

Figure 12. Cytotoxicity of PEG-*b*-PMOEP (○) and ExGen500 (●) at various polymer concentration in HeLa cells. Each error bar represents the standard deviation (n = 3).

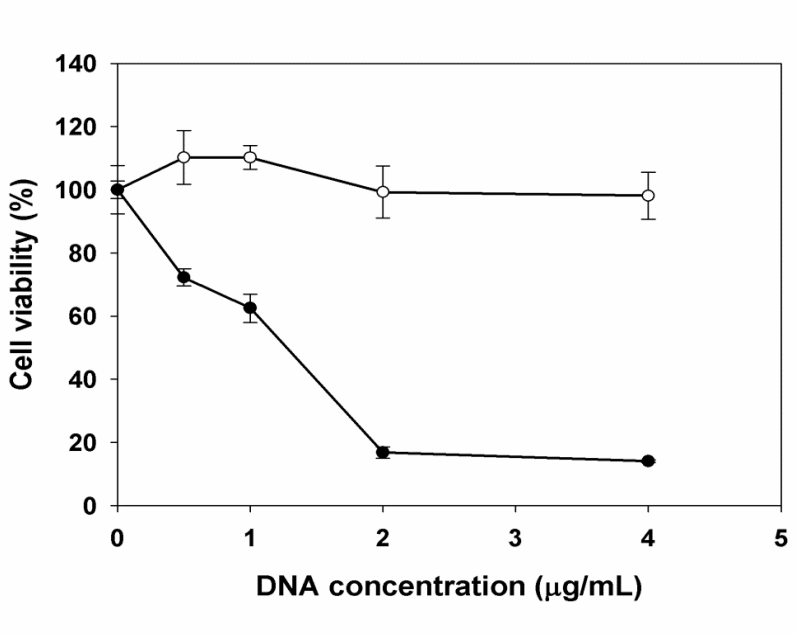

Figure 13. Cytotoxicity of CaPN 2 (○) and ExGen 500/DNA polyplex (N/P=6) (●) at various pDNA concentration in HeLa cells. Each error bar represents the standard deviation (n = 3).

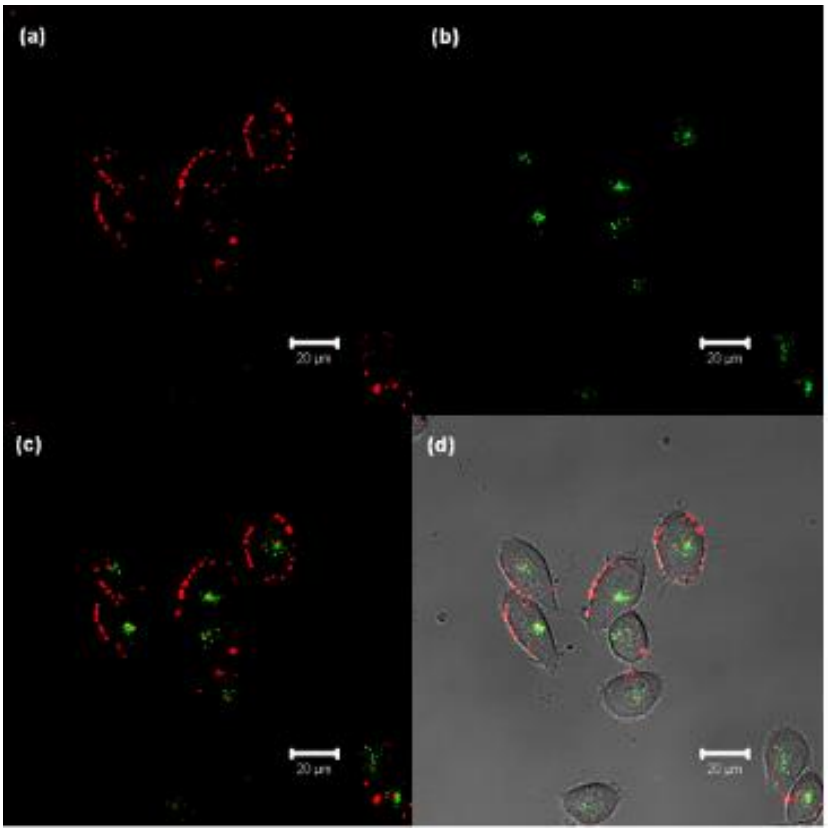

Figure 14. CLSM images of Hela cells transfected with CaP normal (a, b, c, and d). All are images after 24 hr of transfection. (a) are fluorescence images of Cy5-labeled pDNA (red). (b) are fluorescence images of late endosome and lysosome (Green). (c) are merged images of red and green fluorescence. (d) are merged images of DIC and fluorescence.

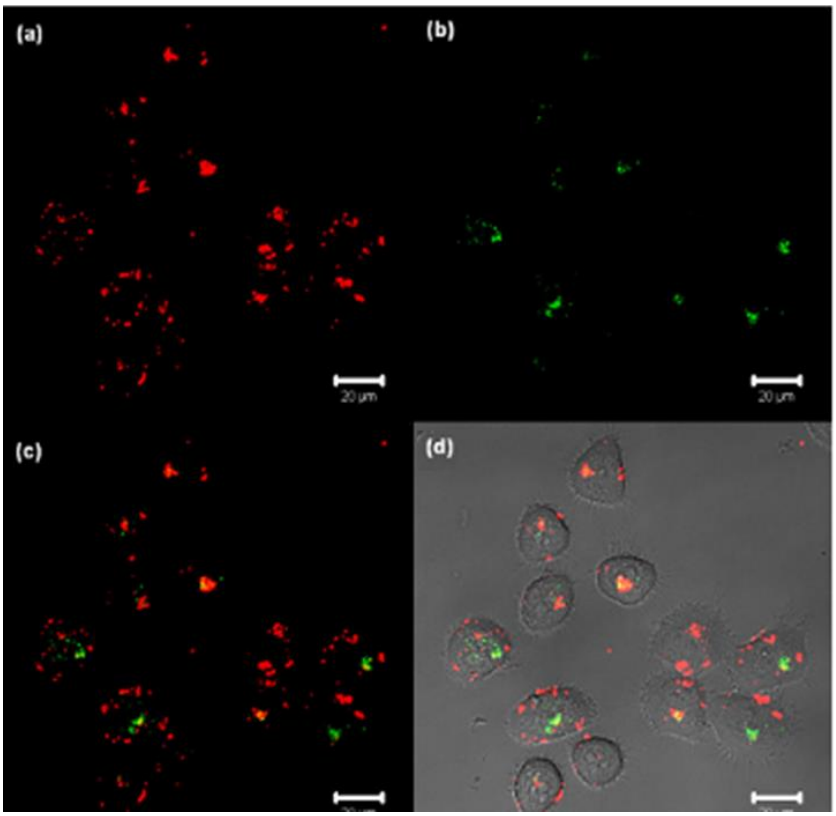

Figure 15. CLSM images of Hela cells transfected with CaPN2 (a, b, c, and d). All are images after 24 hr of transfection. (a) are fluorescence images of Cy5-labeled pDNA (red). (b) are fluorescence images of late endosome and lysosome (Green). (c) are merged images of red and green fluorescence. (d) are merged images of DIC and fluorescence.

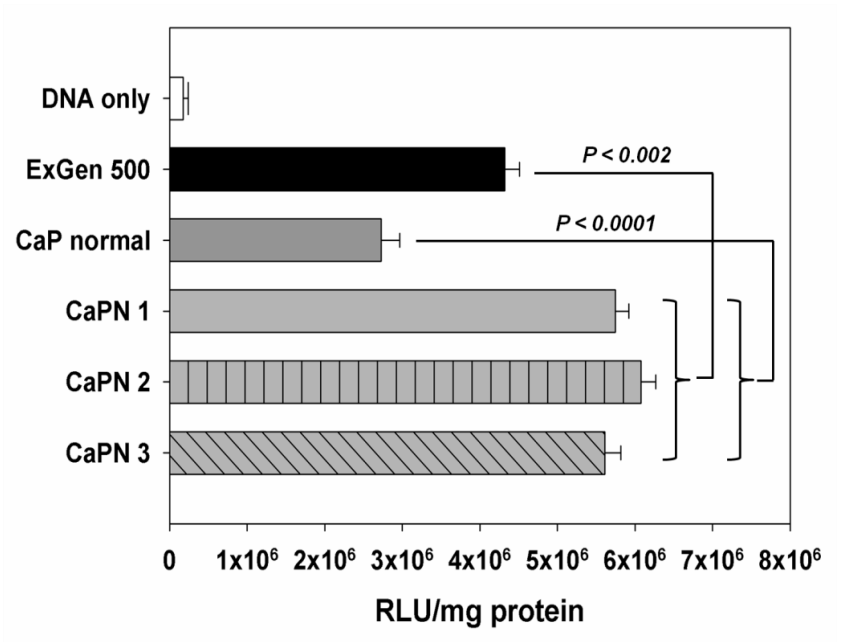

Figure 16. Transfection efficiency of PEG-*b*-PMOEP/CaP nanoparticles in HeLa cells at a pDNA concentration of 1.39 μg/mL. (PEG-*b*-PMOEP concentration of CaPN 1, CaPN 2, CaPN 3 = 380, 440, and 500 μg/mL, respectively). Statistical significance was represented as p value. Error bars indicate the standard deviation (n =3).

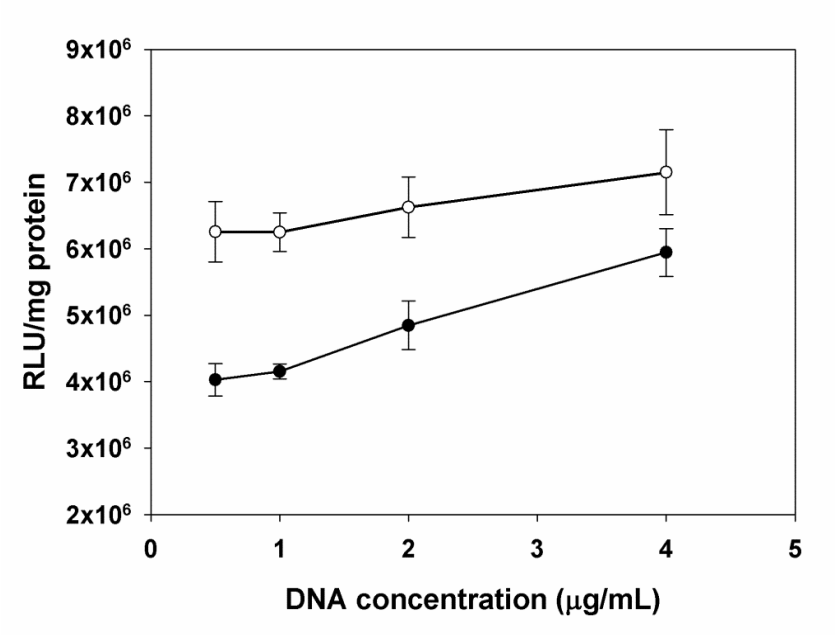

Figure 17. Transfection efficiency of PEG-*b*-PMOEP/CaP nanoparticles (CaPN 2) (○) and ExGen 500 (N/P=6) (●) at various pDNA concentration in HeLa cells. Error bars indicate the standard deviation (n =3).

Table 1. Measurement of molecular weights of polymers

	M_{n1}[a]	M_{n2}[b]	M_w[b]	PD (M_w/ M_n)[b]
PEG-Br initiator (**3**)	5.15×10^3	4.95×10^3	5.10×10^3	1.03
PEG-*b*-PMOEP (**6**)	1.56×10^4	1.72×10^4	1.82×10^4	1.06

[a] The values are determined from ^{1}H NMR spectra.

[b] The values are determined by GPC.

Part II. Delivery of antiviral peptide drugs using dimeric α-helical cell-penetrating peptides with cell penetration activity

1. Abstract

Cell-penetrating peptides (CPPs) are widely used as a non-viral delivery carrier due to their ability to penetrate cell membranes at micromolar concentrations. However, the short- or long-term usage of micromolar CPPs can result in incomplete cell penetration or significant cell membrane damage, respectively. To overcome these drawbacks, dimeric α-helical cell-penetrating peptides (DHCPPs) consisting of leucines (L) and lysines (K) were constructed for efficient cellular uptake even at concentrations in the nanomolar range. Among these LK peptides, LK-3, which was linked by two-disulfide bonds, exhibited a high binding affinity and good chemical stability for the TAR RNA of HIV-1, as reported in the previous study. The monomeric LK peptide (LK-2) with nanomolar affinity was generated after the cleavage of a disulfide bond of LK-3 under the reductive conditions of the cytosol and could bind specifically to TAR RNA. In addition, LK-4 linked by two *N,N'*-1,4-phenylenedimaleimide linkers for maintaining the dimeric form under the cytosolic reductive condition was also synthesized.

It was found that the LK peptides played an essential role in inhibiting the Tat-TAR interaction in cells through efficient cell penetration. Human

immunodeficiency virus-1 (HIV-1) contains a short hairpin RNA, named TAR, which participates in the transcription elongation by interacting with the viral Tat protein. So far, no pharmaceutical agents for inhibiting the Tat-TAR interaction have been commercialized. As short amphipathic α-helical peptides containing leucine and lysine residues show single digit nanomolar affinities for TAR, they can be used as a potential inihibitor of the Tat-TAR interaction. However, most of the peptides have extremely low cell-penetrating abilities. Moreover, significant differences are present in their K_d values for *in vitro* binding and in the effective concentrations determined by the cell-based assays. The LK dimers exhibit a low toxicity at nanomolar concentrations. They can nearly quantitatively penetrate mammalian cells and effectively inhibit the elongation of the TAR transcript. The effective inhibition of HIV-1 replication in T-lymphoblastoid cells strongly suggests that the LK dimers, especially LK-3, have demonstrated the great potential for use as an anti-HIV-1 drug.

2. Introduction

Cell-penetrating peptides (CPPs) are defined as short, hydrophilic or partially hydrophobic, and polybasic peptides with a net positive charge at physiological pH 7.4.[1] Normally, CPPs such as oligoarginine[2], tat[3], penetratin[4], and transportan[5] are able to penetrate the cell membrane at micromolar concentrations in cells. In this study, I employed two sequences of a model amphipathic peptide (MAP) consisting of leucines (L) and lysines (K), which was an unknown CPP, for efficient cell penetration at the nanomolar concentration level. This LK peptide was originally *de novo* designed for use as a calmodulin modulator. Furthermore, I synthesized dimeric α-helical cell-penetrating peptides (DHCPPs) through dimerization by using a peptide stapling technique.[6] The dimeric LK-3 peptide showed a good chemical stability and high α-helix propensity. Once it reaches to cytosol, the LK dimer (i.e., LK-3) is readily reduced, leading to the production of a nanomolar-affinity monomer (i.e., LK-2), which can bind to a short hairpin TAR RNA.[27] In addition, a non-reducible LK-4 dimer linked by two *N,N'*-1,4-phenylenedimaleimides for maintaining the dimeric form under the cytosolic reductive condition was also synthesized.

RNA structure is used as a control element in most biological systems.[7] This is especially true in prokaryotes and viruses where various types of hairpin RNAs control gene expression in the form of riboswitches[8-9] or transcription termination factors.[8-11] Human immunodeficiency virus-1 (HIV-1) contains a short hairpin RNA, named TAR, located in the long terminal repeat (LTR)

region that participates in efficient transcription of the integrated genome.[12-15] Specifically, the interaction between TAR RNA and the viral Tat protein activates transcription of viral genes.[13-16] Consequently, this interaction is a plausible target in developing substances that destroy HIV-1.[17-18] Although this possibility has already been recognized, no pharmaceutical agents that inhibit Tat binding to hairpin RNA-proteins have been commercialized thus far. The likely reason for this lies in the fact that cell-penetrable small molecules[19-21] ineffectively bind to hairpin RNA and the poor cell penetrating potentials of large molecules that efficiently inhibit the Tat-TAR interaction.[22]

Peptides are attractive biomaterials that can be employed to inhibit the Tat-TAR interaction. Owing to this potential, Tat derived peptide fragments, as well as cyclized and more extended analogs of Tat have been explored to assess their competitive binding affinities against hairpin RNA.[23-26] Members of a recently updated list of these peptides were shown to possess single digit nanomolar affinities against TAR[27-28], suggesting that they are potential candidates as HIV-1 targeted therapeutic drugs. However, although Tat is a well-known cell penetrating peptide (CPP)[29-30], the cell permeabilities of Tat analogs are insufficiently low when in-cell concentrations in the nanomolar range are required. Owing to the weak cell penetrating activities of these peptides, significant differences exist between K_d values arising from in vitro binding and cell based assays.

Recently, I observed that a strong correlation exists between α-helicities and cell penetrating activities of amphipathic peptides composed of leucines (L) and lysines (K). Furthermore, I constructed dimeric bundle amphipathic peptides,

which contain two cysteine for leucine replacements per monomer located at the *i* and *i*+7 positions on the hydrophobic face and two disulfide bonds connecting the cysteine residues.[27] Compared to their monomeric counterparts, the dimeric peptides display higher α-helicities as well as stronger affinities against hairpin RNA targets that correspond to sub-nanomolar K_d values. In a more recent effort, the results of which are the focus of this letter, I observed that these dimeric peptides serve as inhibitors of the Tat-TAR interaction involved in transcription in mammalian cells and of HIV-1 replication. In addition, the amphipathic characteristics and high α-helicities of the dimeric peptides leads to high cell penetrating activities and, consequently, the peptides are effective intracellular inhibitors of HIV-1 transcription. Their high cell penetration and TAR RNA binding abilities not only make these peptides the first agents that inhibit transcription of the integrated HIV-1 genome, but also the first peptides that serve as key leads in the search for drugs used in the treatment of HIV-1.

3. Materials and Methods

3.1. Materials

N-α-Fmoc protected L-amino acids, Rink Amide MBHA resin (0.064 mmol/g loading), and benzotriazole-1-yl-oxy-tris-pyrrolidino-phosphonium hexafluorophosphate (PYBOP) were purchased from Novabiochem (San Diego, CA, USA). Dimethylformamide (DMF), Dimethyl sulfoxide (DMSO), 1,2-dichloromethane (DCM), *N,N*-diisopropylethylamine (DIPEA), trifluoroacetic acid (TFA), triisopropylsilane (TIS), piperidine, wortmannin, and amiloride were purchased from Sigma-Aldrich (St. Louis, MO, USA). *N,N'*-1,4-phenylenedimaleimide and 1,2-ethanedithiol (EDT) were purchased from TCI (Japan). N-hexane and diethyl ether were purchased from DAEJUNG (Siheung, Gyeonggi, Korea). All primers and oligonucleotides were purchased from Cosmogenetech (Seoul, Korea). Lipofectamine™ 2000 and Fluorescein-5-Isothiocyante (FITC 'Isomer I'), Trizol, and Superscript II reverse transcriptase were purchased from Invitrogen (Carlsbad, CA, USA). Hoechst 33342 solution was purchased from Dojindo (Japan). The Micro BCA™ Protein Assay Kit and LDH Assay Kit were purchased from Pierce (Rockford, IL, USA). Rotor-Gene SYBR Green RT-PCR Kit was purchased from QIAGEN (Hilden, Germany). pGL2-basic vector was purchased from promega (Madison, WI, USA). pCEP4-Tat plasmid, a TAT expression vector was purchased from Thermo Fisher Scientific (Rockford, IL, USA). For the HIV-1 LTR linked luciferase construct, pHIV-1-LTR-luc, the region from 1 to 644 containing the entire LTR region was amplified with the HIV-1 vector pNL4-3 by polymerase chain reaction by the

use of primers 5'- CGGAGCTCTGGAAGGGCTAATTTGGTCCC-3' (sense strand) and 5'-CGAAGCTTCGGGCGCCACTGCTAGAGAT-3' (antisense strand) and subsequently ligated into the SmaI site of a modified pGL2-basic vector, p(0) via blunt end ligation. A modified p(0) vector has restriction sites with removed sequence between SacI and BglII from pGL2-basic vector.

3.2. Syntheses of peptides

3.2.1. Monomeric peptides

LK-1. Synthesis of LK-1 (sequence: LKKL**L**KLLKKL**L**KLAG) was performed by using an Fmoc-based solid-phase peptide synthesis protocol with Rink Amide MBHA resin. Peptides were synthesized in 64 μmol scale. First of all, Rink Amide MBHA resins (100 mg, 0.059 mmol, 0.064 mmol/g loading) were deprotected with 20% piperidine in DMF (2 mL), and then Fmoc protected first amino acid, glycine (105.2 mg, 0.354 mmol), Benzotriazole-1-yl-oxy-tris-pyrrolidino-phosphonium hexafluorophosphate (PYBOP) (184.2 mg, 0.354 mmol), and *N*,*N*-diisopropylethylamine (DIPEA) (62 μL, 0.354 mmol) was stirred at room temperature for 3 h. The byproducts of reaction were removed with DMF and DCM solvents (3 × 2 mL). The completeness of the reaction was checked by using the 2,4,6-trinitrobenzenesulfonic acid (TNBS) test at coupling step. After coupling step, Fmoc-protected first amino acid was deprotected with 20% piperidine in DMF, and the byproducts of reaction were removed with DMF and DCM solvents (3 × 2 mL). The coupling and deprotection steps were repeated with different Fmoc-protected amino acids sequentially until deprotection of the last Fmoc-protected amino acids. The

deprotected resin-bound peptide was washed with DMF and DCM solvents to remove the piperidine. The N-terminal of this peptide was then acetylated by adding a solution of acetic anhydride (0.3 mmol, 29 μL) and *N*-hydroxybenzotriazole (0.3 mmol, 41 mg) in a solvent (DMF:DCM) (2 mL, v/v= 90:10). The reaction mixtures were stirred for 2 h at room temperature. Cleavage of all peptides from solid support was carried out by treatment with a cleavage mixture consisting of TFA/TIS/EDT/water (2 mL, v/v = 94:1:2.5:2.5) for 2 h at room temperature. The cleaved resin was then separated by filtration and further washed with TFA (1 mL). The separated peptide solution was concentrated by a nitrogen gas. The synthesized peptides were precipitated with the mixture composed of equal volumes of n-hexane and diethyl ether (v/v = 50:50). The resulting suspension was centrifuged at 1,500 rpm for 15 min at room temperature. After the supernatant was carefully decanted, the pellet was dissolved in 0.2 mL of DMSO. All peptides were purified with high-performance liquid chromatography (HPLC, Agilent 1100 series) on a Zorbax C_{18} (3.5 μm, 4.6 × 150 mm) column. The mobile phases used for elution were solution A, which contained 0.1% v/v TFA in water, and solution B, which contained 0.1% v/v TFA in acetonitrile. LK-1 was eluted with a linear gradient of 50–55% with solution B. The peptide was then lyophilized to afford a white powder (4.8 mg, 40% yield). Mass spectra of the peptides were obtained using a Voyager™ MALDI-TOF instrument (Applied Biosystems). The HPLC chromatogram of LK-1 is shown in **Figure 1 (a)** (MS ($M+H^+$): 1861.3 (calcd.), 1862.3 (found); purity > 98% (**Figure 2**)).

LK-2. The same procedure was performed to obtain LK-2 (sequence: LKKL**C**KLLKKL**C**KLAG) as white powder (5.1 mg, 43% yield). The HPLC chromatogram of LK-2 is shown in **Figure 1 (b)** (MS ($M+H^+$):1841.2 (calcd.), 1840.8 (found); purity > 99% (**Figure 3**)).

R9. The same procedure was performed to obtain R9 (sequence: RRRRRRRRR) as white powder (3.6 mg, 38% yield). The HPLC chromatogram of R9 is shown in **Figure 4** (MS ($M+H^+$):1465.0 (calcd.), 1464.5 (found); purity > 99% (**Figure 5**)).

FITC-labeled LK-1. The same procedure was performed to synthesize LK-1 before N-terminal capping. Next, N-terminal fluorescein isothiocyanate (FITC) labeling of LK-1 was performed by using 1.1-fold molar excess of FITC (25.3 mg, 0.065 mmol) and diisopropylethylamine (DIPEA) (42 μL, 0.236 mmol) in 2 mL of dimethylformamide (DMF) for 24 h at room temperature. After cleavage, the peptide was purified using HPLC and then lyophilized to afford a yellow powder (3.3 mg; 23% yield; MS ($M+H^+$): 2208.4 (calcd.), 2208.0 (found)).

FITC-labeled LK-2. FITC-labeled LK-2 was synthesized through the same procedure as mentioned above. After cleavage, the peptide was purified using HPLC and then lyophilized to afford a yellow powder (3.1 mg; 22% yield; MS ($M+H^+$): 2188.2 (calcd.), 2188.5 (found)).

FITC-labeled R9. FITC-labeled R9 was synthesized through the same procedure as mentioned above. After cleavage, the peptide was purified using HPLC and then lyophilized to afford a yellow powder (2.7 mg; 23% yield; MS ($M+H^+$): 1812.0 (calcd.), 1811.7 (found)).

FITC-labeled Tat. FITC-labeled Tat (sequence: AAARKKRRQRRR) was synthesized through the same procedure as mentioned above. After cleavage, the peptide was purified using HPLC and then lyophilized to afford a yellow powder (2.2 mg; 17% yield; MS ($M+H^+$): 1940.0 (calcd.), 1941.2 (found)).

Rhodamine-labeled Rev. Rhodamine-labeled Rev peptide (sequence: TRQARRNRRRRWRERQRAAAAK) was synthesized as a probe peptide for the measurement of RNA-peptide affinity by fluorescence anisotropy. The same procedure was performed to synthesize the Rev peptide before N-terminal capping. And then, N-terminal rhodamine labeling of Rev was performed with 1.1 fold molar excess of 5-carboxy-tetramethylrhodamine (5-TAMRA, 34.3 mg, 0.065 mmol) and DIPEA (42 μL, 0.236 mmol) in DMF (2 mL) for 24 h at room temperature. Remaining procedures were same as mentioned above to obtain the rhodamine-labeled Rev as red powder (MS ($M+H^+$): 3259.8 (calcd), 3259.7 (found)). Concentrations of rhodamine-labeled Rev solutions were determined using the extinction coefficient of rhodamine (ε = 95,000 cm^{-1} M in methanol).

3.2.2. Dimeric peptides

LK-3. Dimerization of LK-2 was performed under air oxidation. For the

synthesis of LK-3, purified N-terminal acetylated monomer (2 mg, 1 μmol) was dissolved in 0.1 M deaerated ammonium bicarbonate (2 mL). The reaction mixture was stirred open to atmosphere for 24 h. The completeness of reaction was checked by HPLC and lyophilized, affording white powder (1.8 mg, 90% yield). The HPLC chromatogram of LK-3 is shown in **Figure 6 (a)** (>99% purity), (MS ($M+H^+$): 3677.4 (calcd.), 3677.9 (found); purity > 99% (**Figure 7**)).

FITC-labeled LK-3. FITC-labeled LK-3 was synthesized through the same procedure as mentioned above from equal amounts of LK-2 (2 mg, 1 μmol) and FITC-labeled LK-2 (2.2 mg, 1 μmol). After cleavage, the peptide was purified using HPLC and then lyophilized to afford a yellow powder (1.9 mg; 45% yield; MS ($M+H^+$): 4024.4 (calcd.), 4024.1 (found)).

LK-4. LK-2 (4 mg, 2.16 μmol) was dissolved in 20 mM sodium phosphate buffer (pH 7.0) (1.2 mL) and *N,N'*-1,4-phenylenedimaleimide (5.8 mg, 21.6 μmol) was dissolved in anhydrous DMF (4.8 mL). The peptide solution was added to the *N,N'*-1,4-phenylenedimaleimide solution and the mixture was stirred at room temperature for 2 h. LK-2 peptide with two maleimide linkers was purified by HPLC and was lyophilized, affording white powder (4.5 mg; 87% yield; MS ($M+H^+$): 2381.3 (calcd.), 2381.7 (found)).

LK-2 (1.6 mg, 0.86 μmol) was dissolved in 20 mM sodium phosphate buffer (pH 7.0) (0.6 mL) and the LK-2 peptide with two maleimide linkers (2 mg, 0.86 μmol) was dissolved in anhydrous DMF (2.4 mL). Two solutions were mixed

and stirred at room temperature for 2 h. The resulting LK-4 dimer was purified by HPLC and was lyophilized, affording yellow powder (3.3 mg, 92% yield). The HPLC chromatogram of LK-4 is shown in **Figure 6 (b)** (MS ($M+H^+$):4172.4 (calcd.), 4172.2 (found); purity > 99% (**Figure 8**)).

FITC-labeled LK-4. FITC-labeled LK-4 was synthesized through the same procedure as mentioned above from equal amount of LK-2 with two maleimide linkers (2 mg, 0.86 μmol) and FITC-labeled LK-2 (1.9 mg, 0.86 μmol). After cleavage, the peptide was purified using HPLC and then lyophilized to afford a yellow powder (1.7 mg; 44% yield; MS ($M+H^+$): 4519.5 (calcd.), 4520.1 (found)).

3.3. Fluorescence Anisotropy (FA) analysis

Fluorescence anisotropy (FA) measurements were performed for the measurement of RNA-peptide affinity by a PerkinElmer LS55 equipped with a thermo-controlled water circulator. Rhodamine-labeled Rev was used as a fluorescence probe. A probe solution (300 nM) was excited at 550 nm and monitored at 580 nm (band path 10 nm each). The integration time was 15 s. Five scans were taken and averaged for each data point. Measurements were performed in a buffer containing 20 mM 4-(2-hydroxyethyl) piperazine-1-ethansulfonic acid (HEPES), 1 mM MgCl2, 5 mM KCl, and 140 mM NaCl (pH 7.4). Competitive binding experiments were performed by adding aliquots of concentrated samples of peptides. A 200 nM rhodamine-REV and 20 nM of TAR solution was titrated with each peptide. The dissociation constant (K_d) was

determined as described previously. The dissociation constant (K_d) of LK-4 was determined to be 0.059 ± 0.007 nM (**Figure 9**). The dissociation constants of LK peptides are summarized in **Table 1.**

3.4. Circular Dichroism (CD) analysis

Measurements of CD spectra were performed using a Chirascan CD spectrometer (Applied Photophysics) with 2.0 mm path-length cell. CD was scanned from 195 to 260 nm, with 0.2s integration, 1 nm step resolution, and 1 nm bandwidth. The results from three scans were averaged.

α-helicities of peptides were measured in a phosphate buffered saline (PBS) (1.47 mM KH_2PO_4, 9.1 mM Na_2HPO_4, 0.9 mM $CaCl_2$, 2.67 mM KCl, 138 mM NaCl, pH 7.4) as a normal condition, a PBS solution with 5mM glutathione (GSH) as a reductive cytosolic condition, and a PBS solution with 50% 2,2,2,trifluoroethanol (TFE) as a membrane-mimic condition at room temperature (Figure S1). For estimation of α-helicity, the averaged CD spectra were analyzed using CDNN (version 2.1), a deconvolution software. The α-helicities are summarized in **Table 1** and **Figure 10.**

3.5. Statistical analysis

All statistical analysis was performed using a t-test between individual treatment groups, using the Graphpad Prism 6.0 software (GraphPad software Inc.).

3.6. Fluorescence Activated Cell Sorting (FACS) analysis

HeLa cells (human cervical cancer cells) (150,000 cells/well) or RAW 264.7 cells (mouse leukaemic monocyte macrophage cells) (150,000 cells/well) were seeded at 24-well plates in DMEM medium supplemented with 10% FBS. After 24 h incubation, the culture medium was replaced with fresh medium with 10% FBS. Each FITC-labeled peptide was diluted in the Opti-MEM buffer, stabilized for 10 min, and added to the cells. After 12 h incubation at 37˚C, the medium was removed and cells were rinsed three times with PBS. Cells were then incubated with trypsin-EDTA for 5 min and detached from the wells. The detached cells were collected by centrifugation at 1,500 rpm. The cells were resuspended in 500 μL PBS containing 2% FBS and 0.1% sodium azide. The cellular uptake of the FITC-labeled peptides was analyzed by FACS Aria II with an excitation wavelength of 488 nm (Becton Dickinson, Mountain View, CA). FITC positive (+) cellular uptake (%) was defined as the percentage of FITC-uptaked cells among all counted cells (30,000 cells) within a pre-fixed gate region. Triplicate experiments were performed for each sample. All FACS data were analyzed using flowjo (Treestar Inc.) software.

For the mechanism study, endocytosis inhibitors (15 μg/ml of amiloride or 50 μg/ml of wortmannin) were treated to the cells for 2 h prior to the addition of peptides. For the low-temperature treatment, the cells were incubated for 4 h at 4˚C.

3.7. Confocal Laser Scanning Microscopy (CLSM) observation

HeLa cells (human cervical cancer cells) (5,000 cells/well) were cultured in

300 μL of DMEM supplemented with 10% FBS on 35-mm glass-base dishes (SPL Lifesciences, South Korea) at 37˚C in a humidified 5% CO_2 incubator. After 24 h, the medium was exchanged with fresh one and FITC-labeled peptides (final 10 nM, 100 nM) were added to the dish and further incubated for 12 h. Nucleus was stained with Hoechst 33342 solution (4 μM) for 10 min prior to the CLSM imaging. Cells were washed three times with PBS for the removal of peptides outside the cells, and fresh medium was added. CLSM images were acquired using a Zeiss DE/LSM 510 NLO (Carl Zeiss, Germany) with 500× objective (C-Apochromat, Carl Zeiss). Excitation wavelengths were 488 nm (Ar laser) and 633 nm (He-Ne laser) for FITC and Hoechst, respectively.

3.8. mRNA inhibition assay using quantitative RT-PCR

HeLa cells (150,000 cells/well) were seeded in 24-well plates and incubated for 24 h at 37˚C. Cells were co-transfected with 1 μg of pLTR (LTR-containing plasmid) and 1 μg of pTat (Tat expression plasmid) by Lipofectamine™ 2000. After 36 h transfection, the cells were rinsed with PBS and fresh medium was added. Each peptide (diluted in a Opti-MEM buffer) was added and further incubated. After 12 h, total RNA in the cells was extracted by using Trizol reagent according to the manufacturer's instruction. Total RNA concentration was quantified by UV spectrophotometry. The RNA was converted to cDNA by reverse transcriptase. Target sequences were amplified by the following primer pairs: HIV-1 TAR-short (product: 59 bp size); GGG TCT CTC TGG TTA GAC CAG (F) and TGG GTT CCC TAG TTA GCC AGA (R), HIV-1 TAR-long (product: 306 bp size); GGG TCT CTC TGG TTA GAC CAG (F)

and CCT CTA GAG GAT AGA ATG GCG C (R), human β-actin (product: 564 bp size); CTG GGA CGA CAT GGA GAA AA (F) and AAG GAA GGC TGG AAG AGT GC (R), human 18S-rRNA (product: 253 bp size); CAG CCA CCC GAG ATT GAG CA (F) and TAG TAG CGA CGG GCG GTG TG (R). Quantitative RT-PCR analysis was performed using Rotor-Gene Q, a real-time PCR Cycler (Qiagen, Hilden, Germany). For real-time PCR using SYBR green, the reaction mixture (20 μL) including 10 μL of 2× Rotor-Gene SYBR Green PCR Master Mix, 1 μM of forward and reverse primer, 100 ng of template cDNA and RNase-free water was prepared and dispensed into PCR tubes. The PCR reaction was performed as follows: PCR initial activation step (5 min at 95˚C) and two-step cycling (5s at 95˚C, 10s at 60˚C × 40 cycles). Relative mRNA gene expression was determined based on the ΔCt (threshold cycles) value between the gene of interest (TAR-luc) and internal reference genes (TAR, β-actin, or 18S rRNA). The mRNA levels of the interest genes were expressed as the ratio of the interest gene to internal reference gene for each sample.

3.9. Transfection and luciferase inhibition assay

HeLa cells or RAW 264.7 cells were seeded at a density of 30,000 cells/well into 24-well tissue culture dishes in 600 μL of complete medium. After 24 h, cells were co-transfected with 1 μg of pLTR and 1 μg of pTat by Lipofectamine™ 2000. After 36 h transfection, the cells were rinsed with PBS and fresh medium was added. Each peptide (diluted in a Opti-MEM buffer) was added and further incubated. After 12 h, the medium was removed and the cells were washed with PBS. The cells were lysed with 150 μL of the reporter lysis

buffer for 30 min at room temperature. Luciferase activity in the transfected cells was measured using an LB 9507 luminometer (Berthold, Germany). The protein concentration of the lysate was determined using a Micro^{TM} BCA protein assay kit. Luciferase activity was measured as RLU/mg of total protein in the lysate. Relative luciferase activity compared with the control (without peptide treatment) was calculated. Each IC_{50} value was calculated using the GraphPad Prism 6.0 software.

3.10. Cytotoxicity assays

3.10.1 LDH assay

HeLa cells or RAW 264.7 cells (10,000 cells/well) were seeded in 96-well plates and incubated in 100 μL of DMEM medium supplemented with 10% FBS in a humidified 5% CO_2 incubator at 37˚C for 24 h. The culture medium was exchanged to 100 μL of DMEM supplemented with 10% FBS. Each peptide was then added to culture medium. After 12 h incubation at 37˚C, samples were centrifuged at 180 × g, the amount of LDH of each sample was determined using a LDH assay kit according to the manufacturer's protocol. The LDH activity from the amount of a red formazan product, which is directly proportional to the amount of LDH released into the medim. The amount of the formazan was measured from difference of the absorbance at 490 nm and the absorbance at 680 nm using a microplate reader (Molecular Devices Co., Menlo Park, CA). The relative membrane destabilization was calculated by comparison with the LDH activity from the cells treated with 0.1% Triton X-100 as 100% and the activity from the cells treated PBS only as 0%.

3.10.2. MTT assay

HeLa cells or RAW 264.7 cells were seeded in 96-well tissue culture dishes at 5,000 cells/well and incubated in 90 μL of DMEM containing 10% FBS for 24 h. After replacing the medium with fresh complete medium, 30 μL of each peptide sample was added and the cells were further incubated for 24 h. 20 μL of filtered MTT solution (2 mg/mL in PBS) was then added to each well. After incubation for 4 hr at 37˚C, the medium was removed from the wells and 150 μL of DMSO was added to dissolve the formazan crystals. Absorbance was measured at 570 nm using a microplate reader (Molecular Devices Co., Menlo Park, CA, USA) and cell viability was calculated by comparison with untreated control cells.

3.11. HIV-1 viral antigen assay

The MOLT-4/CCR5 cells (1 x 10^5 cells/mL) were infected with HIV-1 (III_B strain) at a multiplicity of infection (MOI) of 0.1 and incubated in the absence or presence of the peptides at 37˚C. After incubation for 3 days, the cells were subcultured at a ratio of 1:5 with the same concentration of peptide and further incubated for 3 days. Then, the culture supernatants were collected, and their p24 antigen levels were determined with a sandwich ELISA kit (ZeptoMetrix, Buffalo, NY). The anti-HIV-1 activity of the peptides in acutely infected cells was based on the inhibition of HIV-1 p24 antigen production in MOLT-4/CCR5 cells infected with HIV-1.

4. Results and Discussion

4.1. Binding affinities and α-helicities of peptides

The current investigation arose from an earlier observation[27-28] that the peptide LKKL**L**KLLKKL**L**KLAG (LK-1, **Table 1**) has a strong binding affinity against short hairpin RNAs. In addition, I found that the amphipathic head-to-head dimeric bundle, LK-3[27], containing two disulfide bonds in the middle of each chain, has a sub-nanomolar affinity against TAR RNA. Based on these findings LK-1 and LK-3 were selected for our continuing studies aimed at the development of anti-HIV-1 peptides. Because the disulfide bonds in LK-3 might be cleaved under cytosolic conditions[27, 31-32], the reduced monomeric peptide, LK-2, was generated for use as a control in this study. Furthermore, the non-reducible dimer, LK-4, in which the peptide chains are linked by two *N*,*N'*-1,4-phenylenedimaleimide moieties, was also prepared. Inspection of the dissociation constants (K_d) for binding of the LK peptides to TAR RNA, which are listed in **Table 1**, shows that LK-3 and LK-4 display about 100-1,000 times stronger affinities than do the monomeric peptides LK-1 and LK-2. In addition, I determined the α-helicities of LK peptides in phosphate buffered saline (PBS; pH 7.4) using a membrane-mimic condition (50% trifluoroethanol (TFE) in the PBS) (**Figure 10**). The data show that the dimeric peptides have significantly higher α-helicities than do their monomeric counterparts. This feature is exemplified by the near 90% α-helical contents of LK-3 and LK-4. To test the chemical stability of the peptides under the cytosolic reductive condition, dimeric LK-3 and LK-4 were incubated at the

intracellular glutathione concentration (5 mM) for 72 h (**Figure 11, Table 2**). The obtained data showed that LK-3 was readily reduced to form the monomer LK-2, and its α-helicity was determined to be *ca.* 30% by circular dichroism (CD) spectroscopy. However, LK-4 retained its dimeric form because of the non-reducible linker and exhibited a similar α-helicity to that of LK-3.

4.2. Comparison between cell penetration activity and membrane destabilization activity by FITC-labeled peptides at a high-concentration in HeLa cells

To screen the optimal condition for the LK peptides to efficiently penetrate cells at nanomolar concentrations, I tested the cell penetration activity of high-concentration (10 μM) LK peptides, R9, and Tat incubated for different durations (1 h and 12 h) by following the procedure described in the previous reports[2-3]. For this purpose, fluorescein isothiocyanate (FITC) labeled LK peptides were incubated with HeLa cells, a human cervical cancer cell line, along with R9, a well-known cell penetrating peptide consisting of nine arginines and Tat, an arginine-rich CPP derived from HIV-1 as controls. The results of fluorescence activated cell sorting (FACS) experiments (**Figure 12 (a)**), which give the percentage of the FITC positive cells. The resulting data showed that, in the case of incubation for 1 h, the dimeric LK peptides showed >90% cellular uptake, whereas monomeric LK-1, R9, and Tat showed >60% cellular uptake. These results suggest that R9 and Tat cannot be completely internalized into cells even at a high concentration of 10 μM, although all peptides can completely penetrate the cells after incubation for 12 h. To

compare the relationship between cell-penetration activity and membrane-destabilization activity of LK peptides, R9, and Tat peptide, their lactate dehydrogenase (LDH) activity was measured after incubation for 1 h and 12 h (**Figure 12 (b)**). The results showed that the LDH activities of dimeric LK-3 and LK-4 incubated for 1 h were not significantly different from those incubated for 12 h, whereas LK-4 showed a LDH activity of *ca.* 10% in both cases. On the other hand, monomeric LK-1, R9, and Tat caused a low membrane damage of below 13% after incubation for 1 h; however, significant membrane damage was observed after incubation for 12 h. These results indicate that the destabilization activity of cell membrane is closely related to the cell-penetration activity of CPPs at micromolar concentrations.

4.3. Cell penetration activity of FITC-labeled peptides in HeLa and RAW 264.7 cells

The mammalian cell penetration abilities of the monomeric and dimeric peptides at nanomolar range were evaluated next. The results of FACS experiments (**Figure 13**) show that the cell penetration activities at all concentrations used in the analysis increase in the following order: R9 < LK-1 and LK-2 < LK-4 < LK-3. At high peptide concentrations (>500 nM), both monomeric and dimeric peptides display almost 100% cell penetration. However, at very low concentrations (10 nM), the dimeric peptides have 70-90% cell penetration levels, whereas the monomeric analogs display only *ca.* 40% penetration efficiencies. The control, R9, has only a minimal cell penetration activity at 10 nM. The combined observations demonstrate that the

cell penetrating abilities of the LK peptides are greatly improved by formation of dimers. Additional findings indicate that the dimeric LK peptides also have greatly improved penetration abilities in a mouse leukemic monocyte macrophage cell line (RAW 264.7) (**Figure 14**) and that significant portions of the LK peptides are delivered into cell nuclei (**Figure 15-16**).

4.4. Cell penetration mechanism of FITC-labeled LK peptides in HeLa cells

In order to gain information about the mechanism used for cell penetration, cell permeabilities of LK peptides were examined under various endocytosis inhibiting conditions. The results show that the mechanism employed is dependent on peptide concentration. At low concentrations (10 nM), cell penetration of all LK peptides are nearly completely inhibited by lowering the temperature to 4℃ or by treatment with endocytosis inhibitors (wortmannin or amiloride) (**Figure 17 (a)**).[33] Thus, it appears that at low concentrations LK peptides are internalized by cells using energy-dependent, endocytic pathways, even though their activities of each LK peptide differ significantly at these concentrations. At high concentrations (500 nM), where all LK peptides display >80% cellular uptake, the cell penetration mechanism varies (**Figure 17 (b)**). For example, wortmannin and amiloride display almost no inhibition of cell penetration by both monomeric LK-2 and dimeric LK-3 and the internalization efficiencies of these peptides remain unchanged even at 4℃. Thus, LK-2 and LK-3 penetrate into cells through an energy independent pathway at high concentrations, neither receptor-mediated endocytosis nor macropinocytosis.

Interestingly, cell penetration of 500 nM dimer LK-4, which contains non-reducible maleimide linkers in place of disulfides, is nearly completely inhibited by either lowering the temperature or by treatment with both endocytosis inhibitors. The results suggest that the higher α-helical contents of dimeric peptides facilitate the energy-dependent cell penetration process at low concentrations, while LK-2 or LK-3 undergo energy independent cell penetration (*e.g.,* hole or carpet formation)[34] at high concentrations. However, LK-4 undergo energy-dependent cell penetration due to the structural difference at high concentrations.

4.5. mRNA inhibition assay by LK peptides in HeLa cells

Because they can be delivered into cells at nanomolar concentrations, the LK peptides were employed in studies designed to determine if they inhibit the viral target inside host cells. A luciferase reporter system was constructed on HeLa cells by co-transfection with pLTR-luc, a plasmid containing a HIV-1 LTR promoter and a firefly luciferase gene, and pTat, a plasmid containing HIV-1 Tat gene.[35] In this system, expressed Tat proteins should interact with TAR RNA in the LTR promoter as an anti-termination factor to promote transcription of the luciferase gene. After 12 h incubation of the reporter cells with the LK peptides, the relative amounts of mRNA were determined by using RT-PCR (**Figure 18-19**). The results show that, compared with those of two house-keeping genes, β-actin and 18S rRNA, the amounts of mRNA in the luciferase gene decreases in a peptide dose dependent manner (**Figure 18**). Moreover, the amount of the long luciferase gene transcript with total TAR RNA transcribed

was evaluated to demonstrate that the LK peptides do not prevent transcription by binding to TAR DNA of transfected plasmid DNA. The ratio of TAR-luc (long transcript) to TAR (total transcript) was found to be similar to the ratio of TAR-luc to mRNA of house-keeping genes. This observation suggests that the Tat-TAR interaction is inhibited by the LK peptides at the transcriptional level (**Figure 19**).

The inhibitory activity against Tat mediated transcription varies among the peptides with monomeric LK-1 and LK-2 exhibiting less than 50% inhibition even at 100 nM. In contrast, dimeric peptides LK-3 and LK-4, which possess higher cell penetration abilities, display ca. 50% inhibition at 10 nM, and more than 80% inhibition at 100 nM. Because the HeLa cell penetration activities of LK-1 and LK-2 are similar (**Figure 13**), the stronger inhibitory effect of LK-2 is likely a consequence of its stronger binding affinity against TAR RNA (**Table 1**). Because disulfide bonds are readily degraded under reductive cytosolic conditions, it is likely that LK-3 is reduced in the cytosol after internalization to form monomeric LK-2 that still binds to the TAR RNA with nanomolar affinity. Therefore, the enhanced cell penetration activity of LK-3 over LK-2 is the main source of its outstanding ability to inhibit the Tat-TAR interaction at the transcriptional level. Although its cell penetration ability is slightly less than that of LK-3, LK-4 displays a similar inhibitory activity as does LK-3 owing to the effect of the non-reducible linker that enables the peptide to retain its dimeric form in the cytosol and high TAR RNA binding affinity.

4.6. Luciferase inhibition assay by LK peptides after transfection of HeLa and RAW 264.7 cells by pLTR and pTat

The IC_{50} values of the LK peptides, determined by using the luciferase assay (**Figure 20-21**), were observed to decrease in the order LK-1 (110 nM) > LK-2 (50 nM) > LK-4 (35 nM) > LK-3 (10 nM). The IC_{50} value of dimeric LK-3, which is more than 10-fold lower than that of monomeric LK-1, is a consequence of its enhanced cell penetration ability as well as the 2-fold increase of monomeric peptide concentration that takes place when LK-3 undergoes cytosolic cleavage. The IC_{50} value of LK-3 is almost same as the dissociation constant of LK-2 (K_d = 9.6 nM), which indicates that cell membrane penetration no longer serves as the barrier for in cell activity, a unique feature not shared by other peptide drugs that display large discrepancies between K_d and IC_{50} values. Similar results (IC_{50} of LK-3 = 18 nM) are also seen in studies using macrophage cells (RAW 264.7) (**Figure 22-23**). Moreover, the inhibition of LK peptides was decreased according to the increase of Tat expression (**Figure 24**). The result also suggests that the competitive binding between Tat and LK peptides on TAR RNA is the main factor for the inhibition.

4.7. Cytotoxicity assays of HeLa and RAW 264.7 cells by LK peptides

Membrane destabilization and cytotoxicities of HeLa and RAW 264.7 cells by LK peptides were determined by using respective LDH and MTT assays (**Figure 25-26**). The results demonstrate that all of the LK peptides do not cause membrane destabilization up to 2 μM concentrations, and only LK-3 brings about a small membrane destabilization at 8 μM. Also, the MTT assay results

show that the LK peptides are not cytotoxic at concentrations below 10 μM, similar to the previous report of oligoarginine peptides.[2] These observations suggest that the high cell penetrating activities of the LK peptides is not caused by plasma membrane disruption, which would induce cell lysis and eventually cell death.

4.8. Anti-HIV-1 activity by LK peptides after HIV-1 infection in T-lymphoblastoid cells

In the final phase of this effort, the inhibitory effects of the peptides on HIV-1 replication in acutely infected T-lymphoblastoid cells (MOLT-4/CCR5)[36] were evaluated (**Figure 27**). The IC_{50} values of LK-3 and LK-4 for HIV-1 replication were 590 and 280 nM, respectively, while the IC_{50} value of LK-1 for HIV-1 replication was >2 μM (data not shown). The larger IC_{50} values, compared with those arising from experiments with HeLa or RAW 264.7 cells, may be partially attributed to the reduced penetration activity of the peptides to T-lymphoblastoid cells. However, LK-3 did not show significant cytotoxicity to the host cells at concentrations up to 2.6 μM, which is considerably higher than its IC_{50} value for HIV-1 replication. LK-4 was found to be more active than LK-3, but it was also more cytotoxic to the host cells (data not shown). These findings suggest that the LK dimers, especially LK-3, have potential as a therapeutic application against HIV-1.

5. Conclusion

In summary, I have demonstrated that α-helical LK dimeric bundles have large cell penetrating abilities and that they target intracellular hairpin RNA. Owing to their *ca.* 90% of helical contents in an aqueous buffer, the LK dimers have significantly enhanced cell penetration activities compared to those of the corresponding monomer. This feature results in near quantitative uptake of dimeric peptides in HeLa and macrophage cells at low nanomolar concentrations. By using RT-PCR and a luciferase reporter assay, I showed that the LK dimers display dose dependent inhibition of the Tat-TAR interaction with IC_{50} values that are *ca.* 10 nM. In addition, the dimeric peptides are not cytotoxic at concentrations <2 μM. The results of experiments using HIV-1-infected cells show that the LK dimeric peptides inhibit viral replication at nanomolar concentration. This finding strongly suggests that the LK dimers have the potential of serving as effective anti-HIV-1 drugs that function by inhibiting the Tat-TAR interaction that takes place in acute phases of the disease.

6. References

1. Milletti, F. Cell-penetrating peptides: classes, origin, and current landscape. *Drug Discovery Today* **17**, 850-860 (2012).

2. Kosuge, M., Takeuchi, T., Nakase, I., Jones, A.T. & Futaki, S. Cellular Internalization and Distribution of Arginine-Rich Peptides as a Function of Extracellular Peptide Concentration, Serum, and Plasma Membrane Associated Proteoglycans. *Bioconjugate Chemistry* **19**, 656-664 (2008).

3. Tréhin, R. et al. Cellular Internalization of Human Calcitonin Derived Peptides in MDCK Monolayers: A Comparative Study with Tat(47-57) and Penetratin(43-58). *Pharmaceutical Research* **21**, 33-42 (2004).

4. Hällbrink, M., Oehlke, J., Papsdorf, G. & Bienert, M. Uptake of cell-penetrating peptides is dependent on peptide-to-cell ratio rather than on peptide concentration. *Biochimica et Biophysica Acta (BBA) - Biomembranes* **1667**, 222-228 (2004).

5. EL-Andaloussi, S., JÄrver, P., Johansson, H.J. & Langel, Ü. Cargo-dependent cytotoxicity and delivery efficacy of cell-penetrating peptides: a comparative study. *Biochemical Journal* **407**, 285–292 (2007).

6. Verdine, G.L. & Hilinski, G.J. Chapter one - Stapled Peptides for Intracellular Drug Targets. *Methods in Enzymology* **503**, 3-33 (2012).

7. Svoboda, P. & Di Cara, A. Hairpin RNA: a secondary structure of primary importance. *Cellular and Molecular Life Sciences* **63**, 901-908 (2006).

8. Deigan, K.E. & Ferre-D'Amare, A.R. Riboswitches: discovery of drugs that target bacterial gene-regulatory RNAs. *Accounts of Chemical Research* **44**,

1329-1338 (2011).

9. Serganov, A. & Nudler, E. A decade of riboswitches. *Cell* **152**, 17-24 (2013).

10. Merino, E. & Yanofsky, C. Transcription attenuation: a highly conserved regulatory strategy used by bacteria. *Trends in Genetics* **21**, 260-264 (2005).

11. Battiste, J.L. et al. Alpha helix-RNA major groove recognition in an HIV-1 rev peptide-RRE RNA complex. *Science* **273**, 1547-1551 (1996).

12. Rosen, C.A., Sodroski, J.G. & Haseltine, W.A. The location of cis-acting regulatory sequences in the human T cell lymphotropic virus type III (HTLVIII/LAV) long terminal repeat. *Cell* **41**, 813-823 (1985).

13. Kao, S.Y., Calman, A.F., Luciw, P.A. & Peterlin, B.M. Anti-termination of transcription within the long terminal repeat of HIV-1 by tat gene product. *Nature* **330**, 489-493 (1987).

14. Berkhout, B., Silverman, R.H. & Jeang, K.T. Tat trans-activates the human immunodeficiency virus through a nascent RNA target. *Cell* **59**, 273-282 (1989).

15. Lu, H., Li, Z., Xue, Y. & Zhou, Q. Viral-host interactions that control HIV-1 transcriptional elongation. *Chemical Reviews* **113**, 8567-8582 (2013).

16. Laspia, M.F., Rice, A.P. & Mathews, M.B. HIV-1 Tat protein increases transcriptional initiation and stabilizes elongation. *Cell* **59**, 283-292 (1989).

17. Darfeuille, F. et al. Loop-loop interaction of HIV-1 TAR RNA with N3'-->P5' deoxyphosphoramidate aptamers inhibits in vitro Tat-mediated transcription. *Proceedings of the National Academy of Sciences* **99**, 9709-9714 (2002).

18. Bannwarth, S. & Gatignol, A. HIV-1 TAR RNA: the target of molecular interactions between the virus and its host. *Current HIV Research* **3**, 61-71

(2005).

19. Tabarrini, O. et al. Studies of anti-HIV transcription inhibitor quinolones: identification of potent N1-vinyl derivatives. *ChemMedChem* **5**, 1880-1892 (2010).

20. Massari, S. et al. A 1,8-naphthyridone derivative targets the HIV-1 Tat-mediated transcription and potently inhibits the HIV-1 replication. *Journal of Medicinal Chemistry* **53**, 641-648 (2010).

21. Manfroni, G. et al. Synthesis and biological evaluation of 2-phenylquinolones targeted at Tat/TAR recognition. *Bioorganic & Medicinal Chemistry Letters* **19**, 714-717 (2009).

22. Wang, D. et al. Multivalent binding oligomers inhibit HIV Tat-TAR interaction critical for viral replication. *Bioorganic & Medicinal Chemistry Letters* **19**, 6893-6897 (2009).

23. Davidson, A. et al. Simultaneous recognition of HIV-1 TAR RNA bulge and loop sequences by cyclic peptide mimics of Tat protein. *Proceedings of the National Academy of Sciences* **106**, 11931-11936 (2009).

24. Friedler, A. et al. Development of a functional backbone cyclic mimetic of the HIV-1 Tat arginine-rich motif. *Journal of Biological Chemistry* **275**, 23783-23789 (2000).

25. Huq, I., Ping, Y.H., Tamilarasu, N. & Rana, T.M. Controlling human immunodeficiency virus type 1 gene expression by unnatural peptides. *Biochemistry* **38**, 5172-5177 (1999).

26. Hamy, F. et al. An inhibitor of the Tat/TAR RNA interaction that effectively suppresses HIV-1 replication. *Proceedings of the National Academy of Sciences*

94, 3548-3553 (1997).

27. Hyun, S., Na, J., Lee, S.J., Park, S. & Yu, J. RNA grooves can accommodate disulfide-bridged bundles of alpha-helical peptides. *ChemBioChem* **11**, 767-770 (2010).

28. Lee, Y., Hyun, S., Kim, H.J. & Yu, J. Amphiphilic helical peptides containing two acridine moieties display picomolar affinity toward HIV-1 RRE and TAR. *Angewandte Chemie International Edition* **47**, 134-137 (2008).

29. Ziegler, A., Nervi, P., Durrenberger, M. & Seelig, J. The cationic cell-penetrating peptide CPP(TAT) derived from the HIV-1 protein TAT is rapidly transported into living fibroblasts: optical, biophysical, and metabolic evidence. *Biochemistry* **44**, 138-148 (2005).

30. Fawell, S. et al. Tat-mediated delivery of heterologous proteins into cells. *Proceedings of the National Academy of Sciences* **91**, 664-668 (1994).

31. Lee, Y. et al. Poly(ethylene oxide sulfide): new poly(ethylene glycol) derivatives degradable in reductive conditions. *Biomacromolecules* **6**, 24-26 (2005).

32. Lee, Y. et al. Visualization of the degradation of a disulfide polymer, linear poly(ethylenimine sulfide), for gene delivery. *Bioconjugate Chemistry* **18**, 13-18 (2007).

33. El-Sayed, A. & Harashima, H. Endocytosis of gene delivery vectors: from clathrin-dependent to lipid raft-mediated endocytosis. *Molecular Therapy* **21**, 1118-1130 (2013).

34. Herce, H.D. & Garcia, A.E. Molecular dynamics simulations suggest a mechanism for translocation of the HIV-1 TAT peptide across lipid membranes.

Proceedings of the National Academy of Sciences **104**, 20805-20810 (2007).

35. Pai, J. et al. High-throughput profiling of peptide-RNA interactions using peptide microarrays. *Journal of the American Chemical Society* **134**, 19287-19296 (2012).

36. Baba, M., Miyake, H., Okamoto, M., Iizawa, Y. & Okonogi, K. Establishment of a CCR5-expressing T-lymphoblastoid cell line highly susceptible to R5 HIV type 1. *AIDS Research and Human Retrovirus* **16**, 935-941 (2000).

(a)

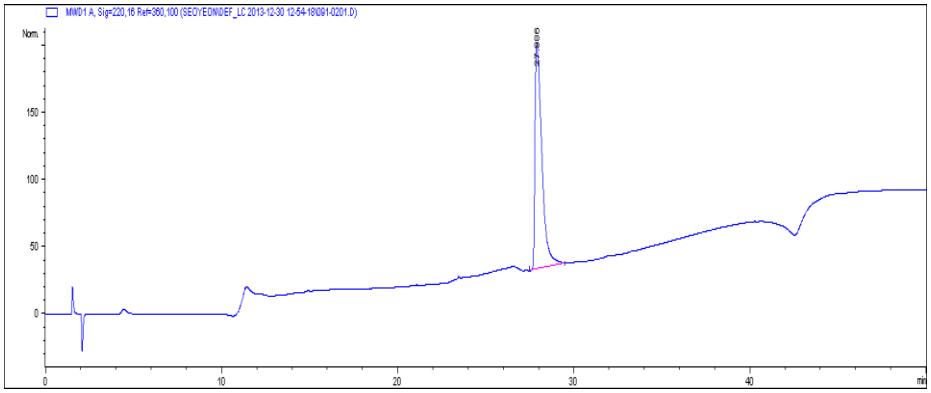

(b)

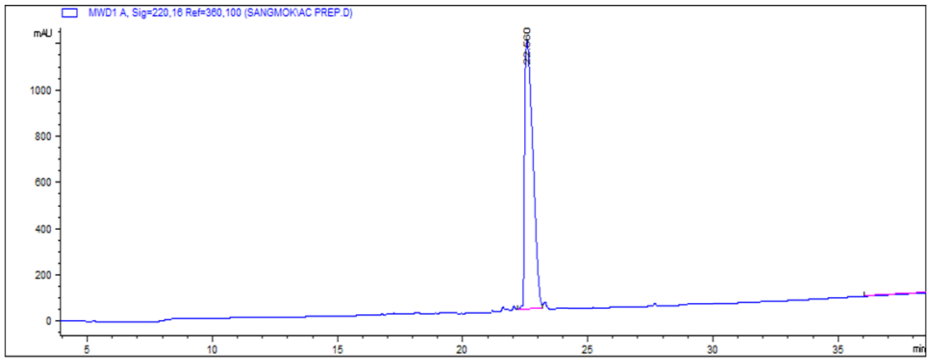

Figure 1. HPLC chromatogram of (a) LK-1 and (b) LK-2 peptides

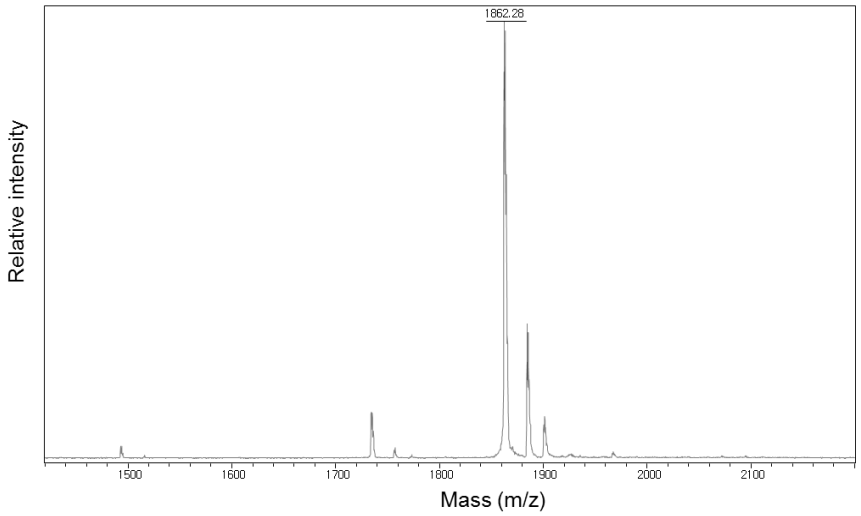

Figure 2. Maldi-TOF mass spectra of LK-1 peptide

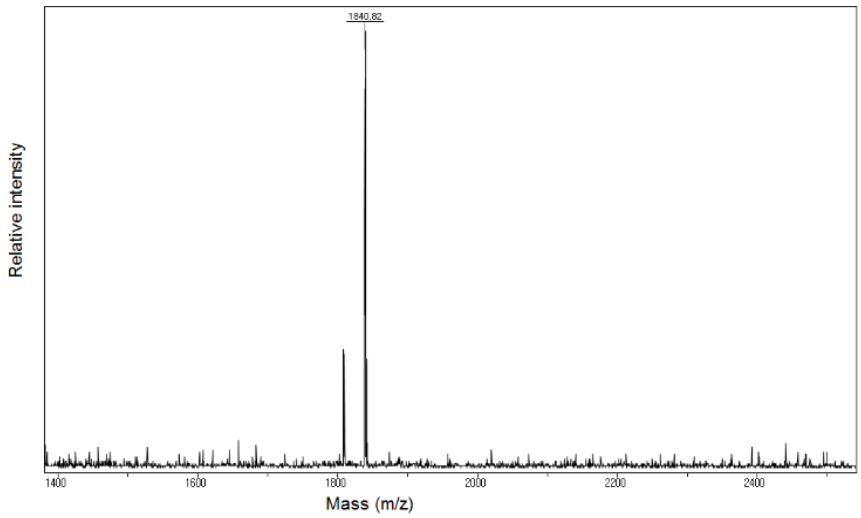

Figure 3. Maldi-TOF mass spectra of LK-2 peptide

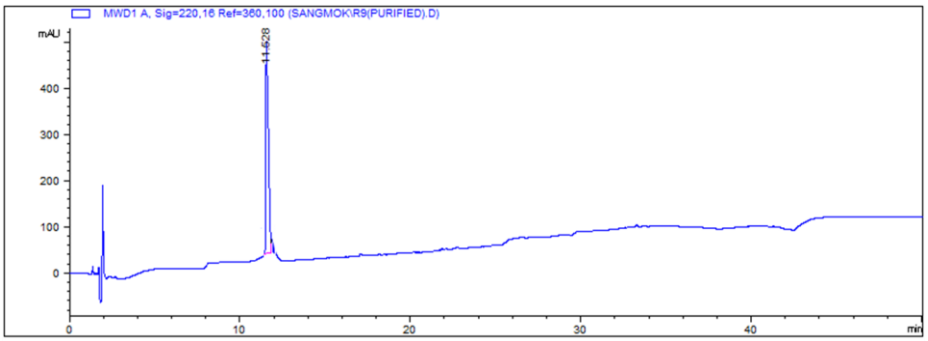

Figure 4. HPLC chromatogram of R9 peptide

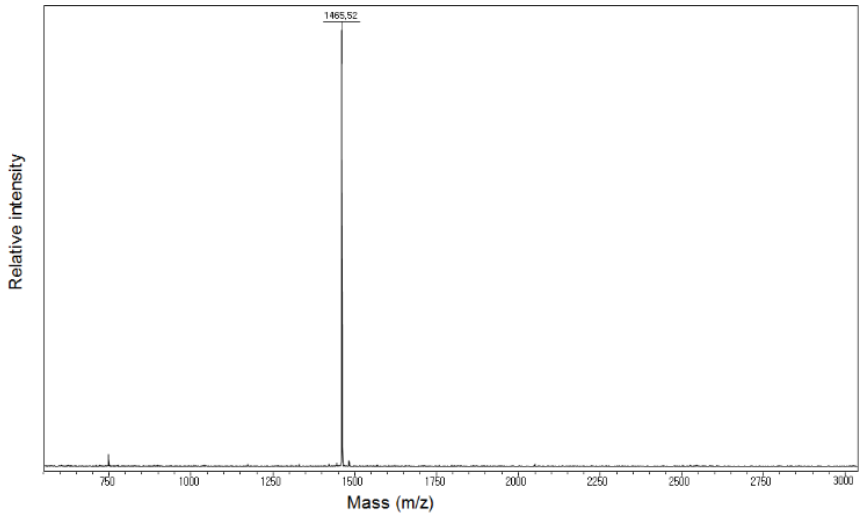

Figure 5. Maldi-TOF mass spectra of R9 peptide

(a)

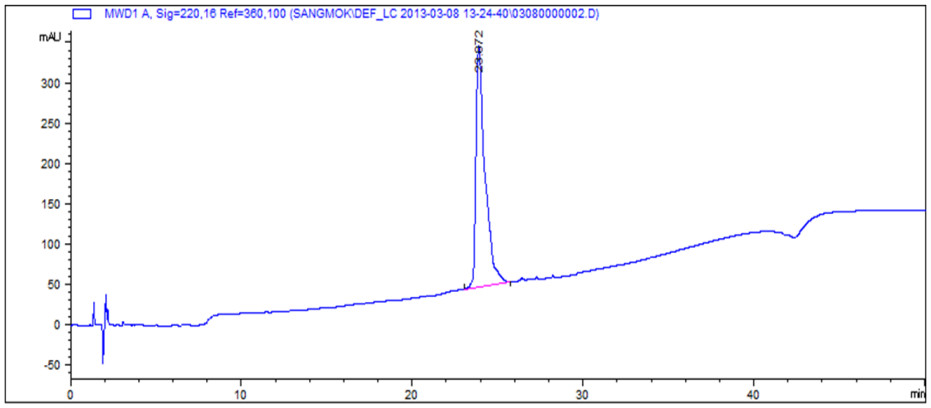

(b)

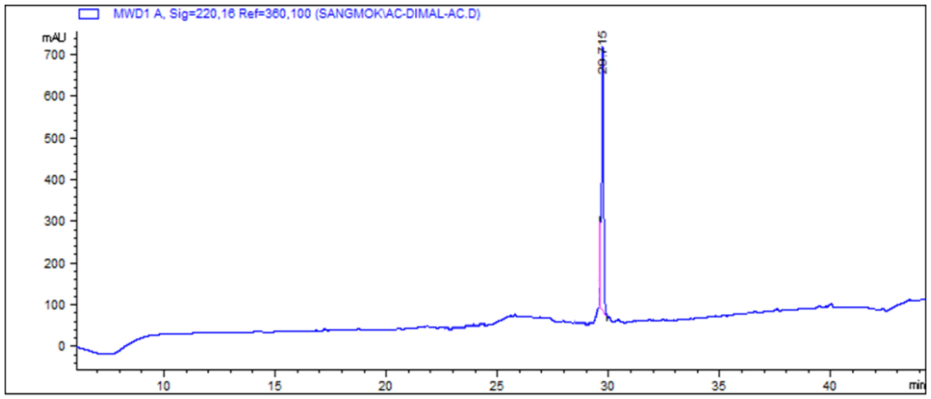

Figure 6. HPLC chromatogram of (a) LK-3 and (b) LK-4 peptides

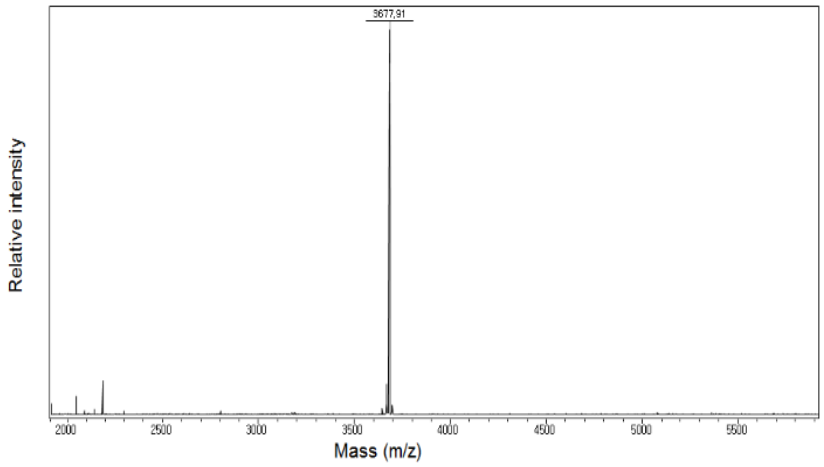

Figure 7. Maldi-TOF mass spectra of LK-3 peptide

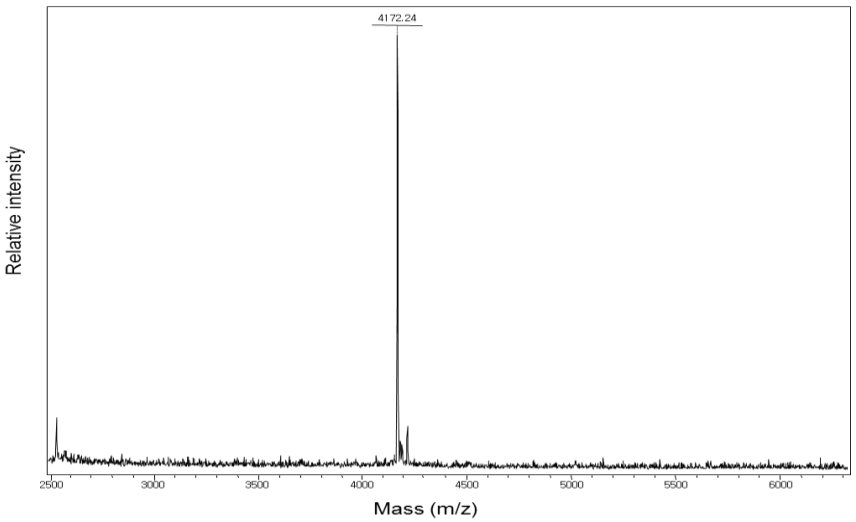

Figure 8. Maldi-TOF mass spectra of LK-4 peptide

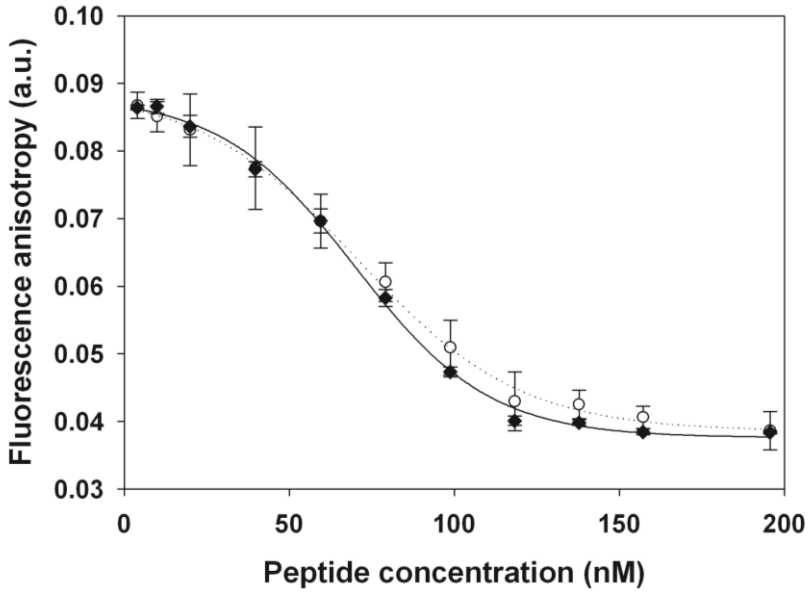

Figure 9. FA experiments for the measurement of binding affinity of LK-3 and LK-4 against TAR RNA. The FA values from the titration with LK-3 and LK-4 are shown as the dotted line with open circles and the solid line with diamonds, respectively. Each error bar represents the standard deviation (n = 3).

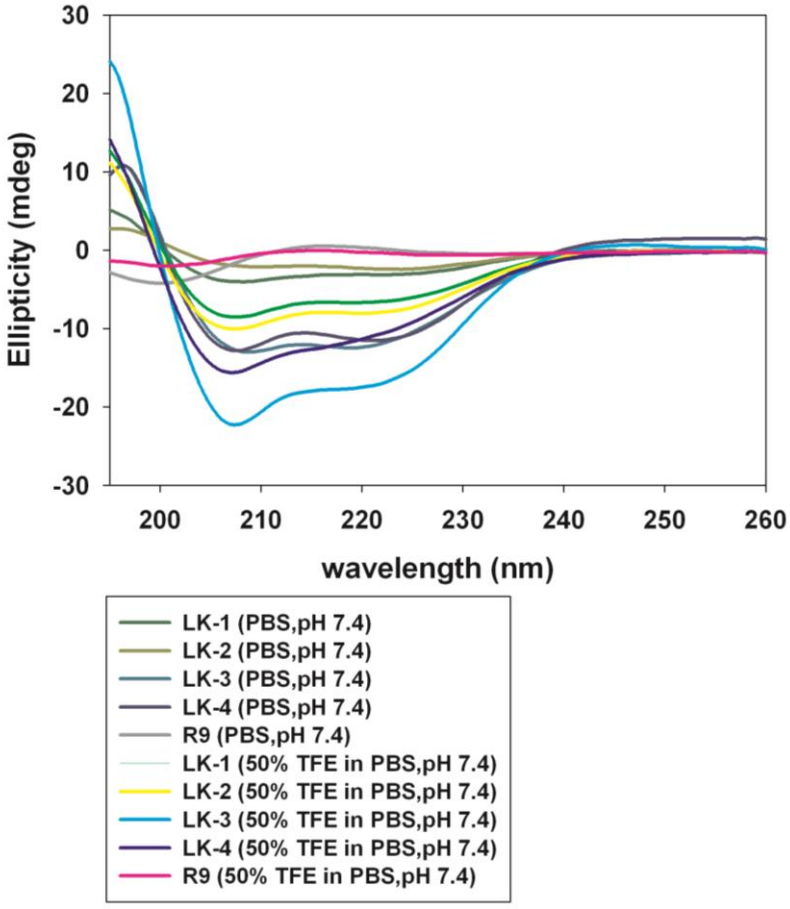

Figure 10. CD spectra of peptides in PBS and 50% TFE in PBS. The concentration of each peptide was 100 μM.

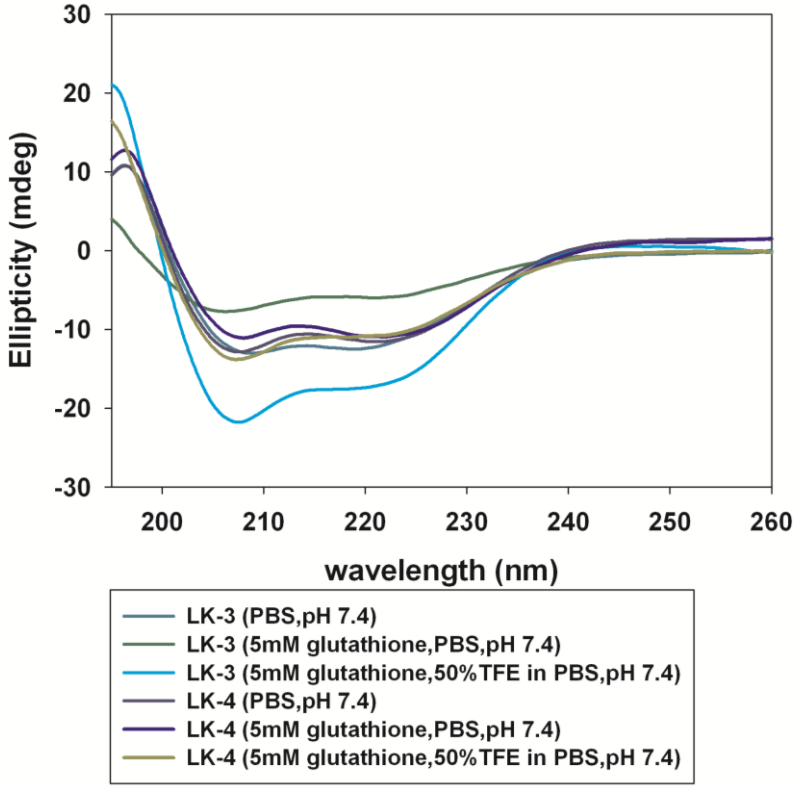

Figure 11. CD spectra of dimeric peptides in presence of glutathione. The concentration of each peptide was 100 μM.

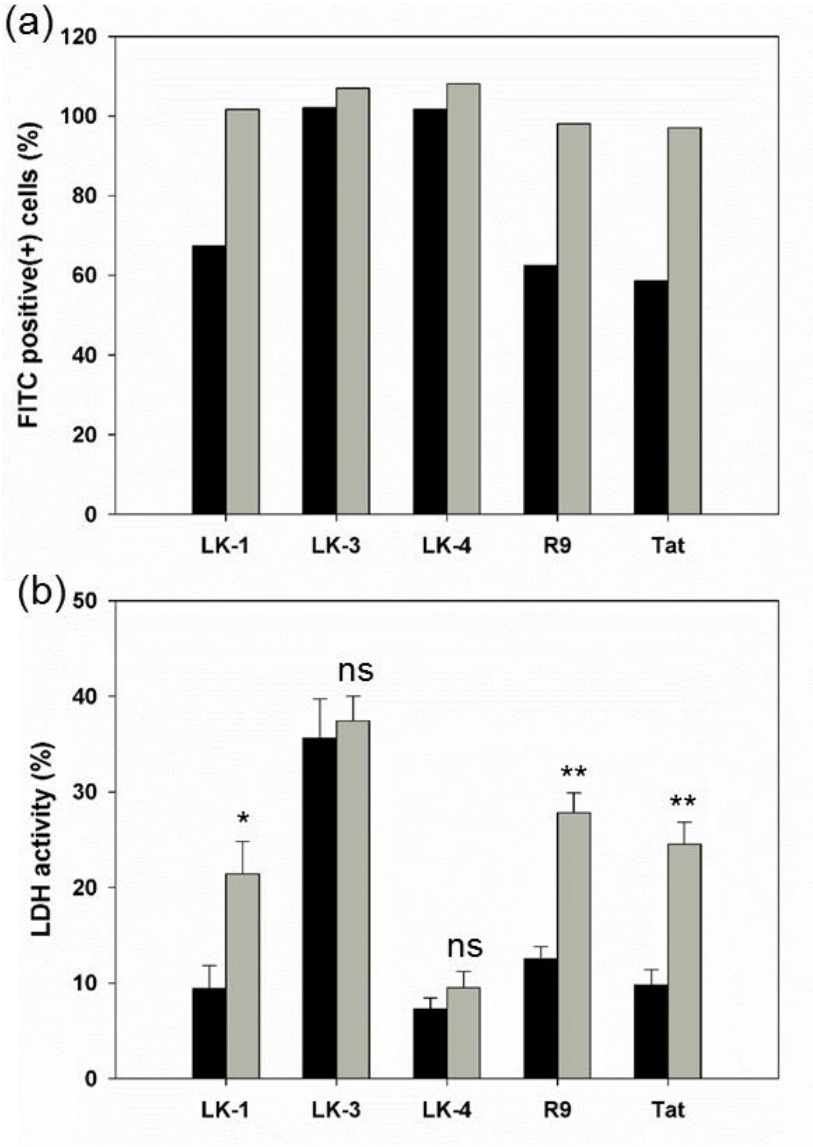

Figure 12. Comparison between (a) cell penetration activity and (b) membrane destabilization activity by peptides. 1 h incubaion (black), 12 h incubaion (gray). Each error bar represents the standard deviation (n = 3). The markers (*), (**), and (ns) indicate $0.01 \leq p < 0.1$, $0.001 \leq p < 0.01$ and no significant difference compared with 1 h incubation, respectively.

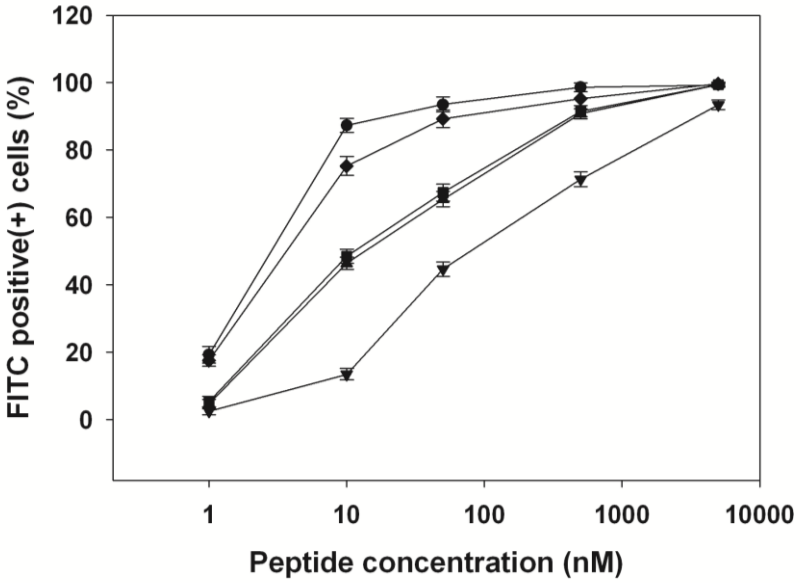

Figure 13. FACS results for LK-1 (▲), LK-2 (■), LK-3 (●), LK-4 (♦), and R9 (▼) at various peptide concentrations in HeLa cells.

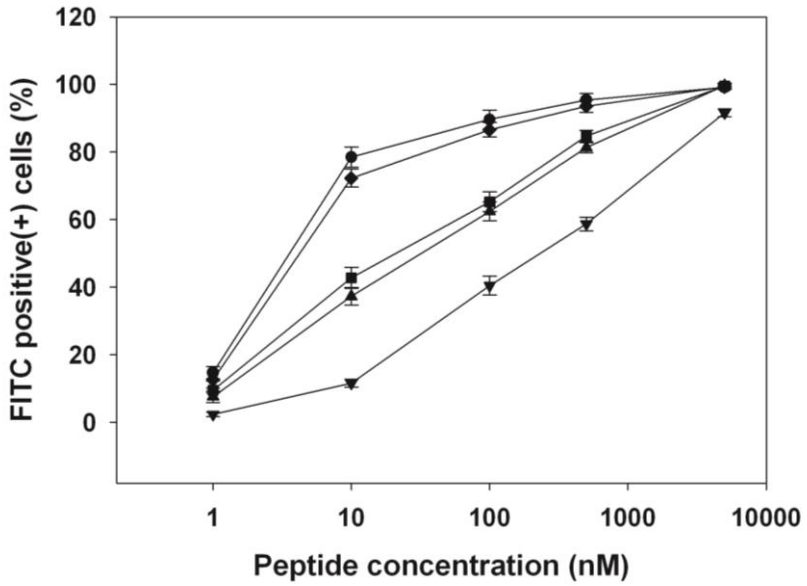

Figure 14. FACS results for LK-1 (▲), LK-2 (■), LK-3 (●), LK-4 (♦), and R9 (▼) at various peptide concentrations in RAW 264.7 cells.

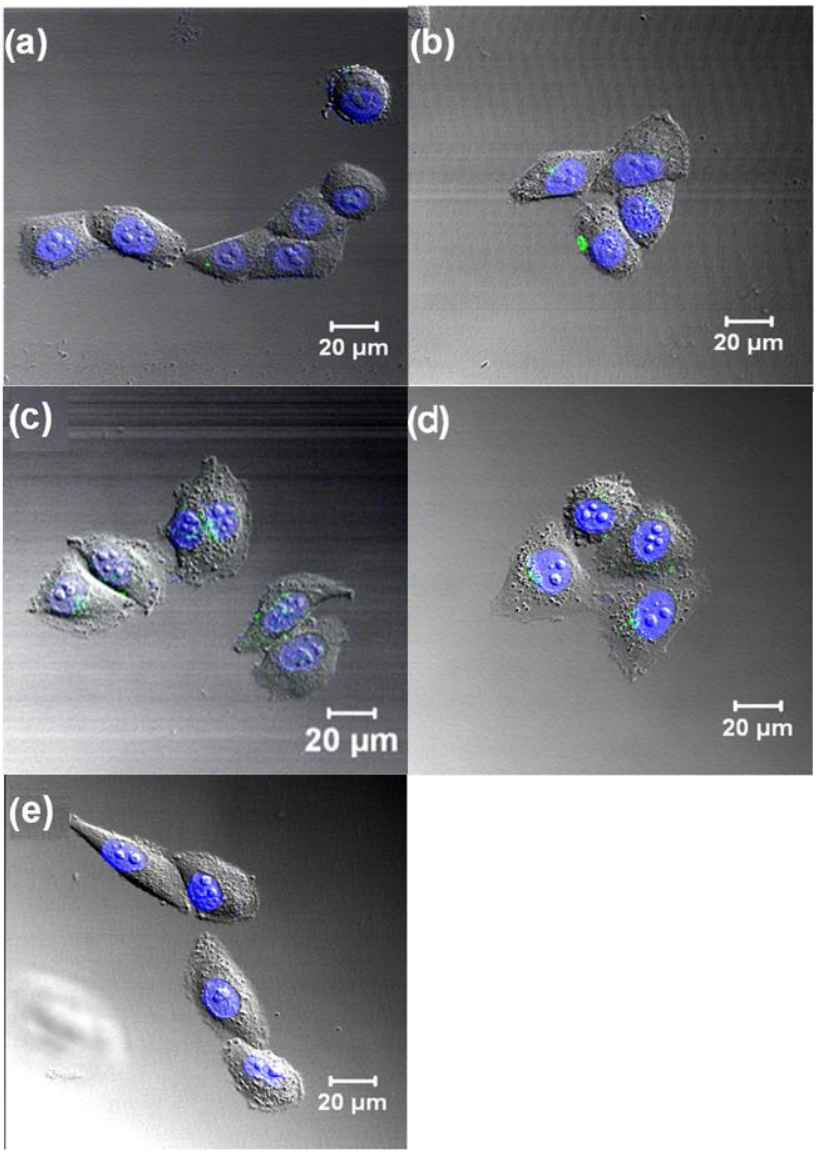

Figure 15. CLSM images of HeLa cells after 12 h treatment of FITC-labeled (a) LK-1, (b) LK-2, (c) LK-3, (c) LK-4, and (d) R9 peptide at 10 nM. Nucleus was stained with Hoechst 33442 (blue).

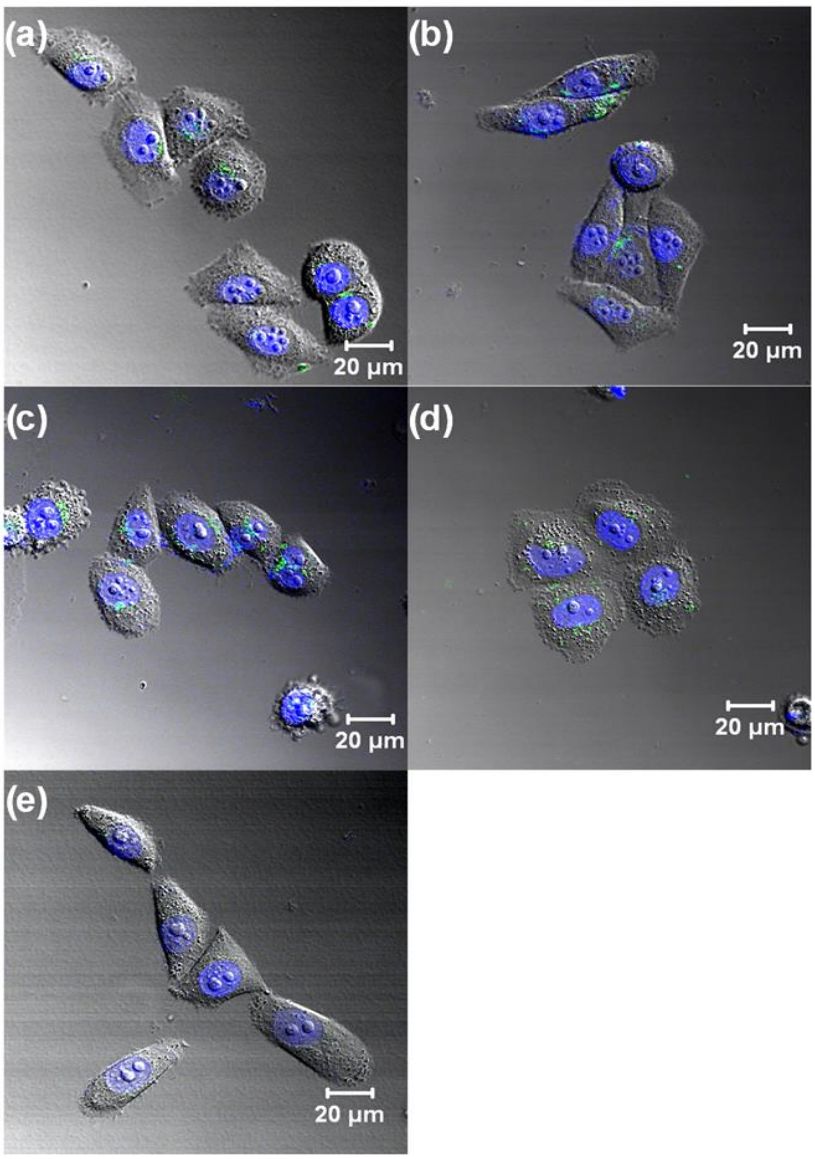

Figure 16. CLSM images of HeLa cells after 12 h treatment of FITC-labeled (a) LK-1, (b) LK-2, (c) LK-3, (d) LK-4, and (e) R9 peptide at 100 nM. Nucleus was stained with Hoechst 33442 (blue).

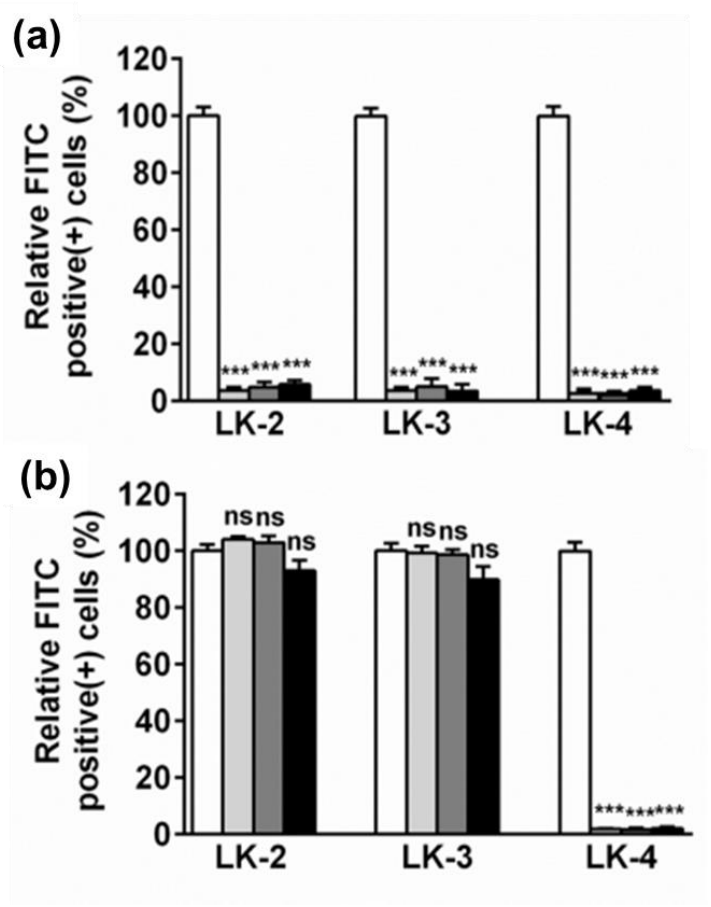

Figure 17. The relative cell penetration activity of LK peptides at endocytosis-inhibiting conditions at (a) 10 nM and (b) 500 nM in HeLa cells after 12 h incubation. Control (white), wortmannin (gray), amiloride (dark gray), and 4˚C (black). Each error bar represents the standard deviation (n = 3). The markers (***) and (ns) indicate $p<0.001$ and no significant difference compared with the control, respectively.

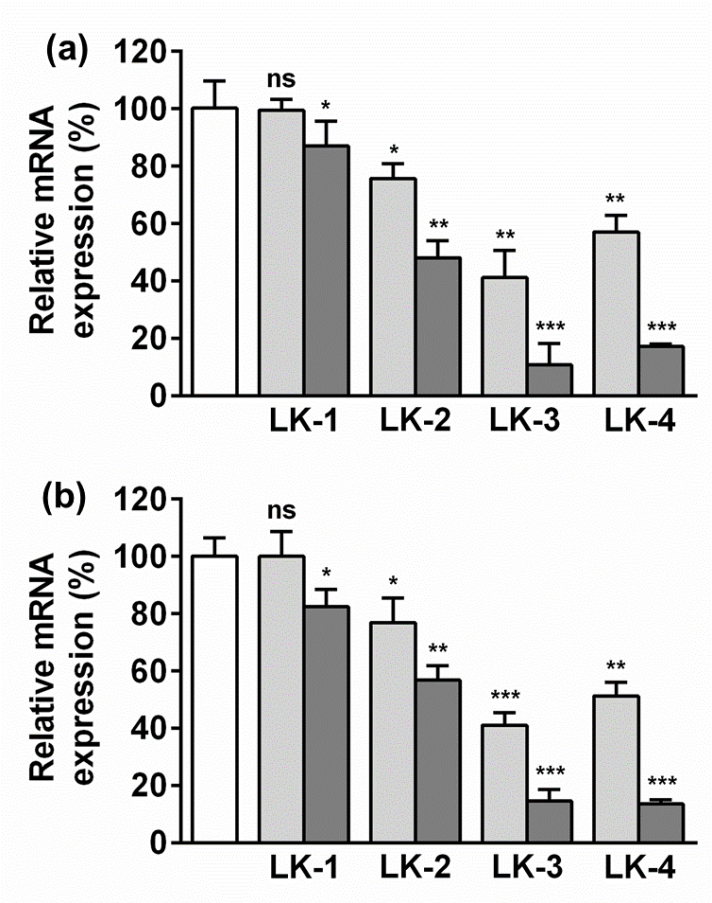

Figure 18. Inhibition of the Tat-mediated transcriptional elongation by LK peptides in HeLa cells. Relative mRNA expression of (a) TAR-luc/β-actin, (b) TAR-luc/18S rRNA at 10 nM and 100 nM of each LK peptide. Control (white), 10 nM (gray), 100 nM (dark gray). Each error bar represents the standard deviation (n = 3). The markers (*), (**), (***), and (ns) indicate $0.01 \leq p < 0.1$, $0.001 \leq p < 0.01$, $p < 0.001$ and no significant difference compared with control, respectively.

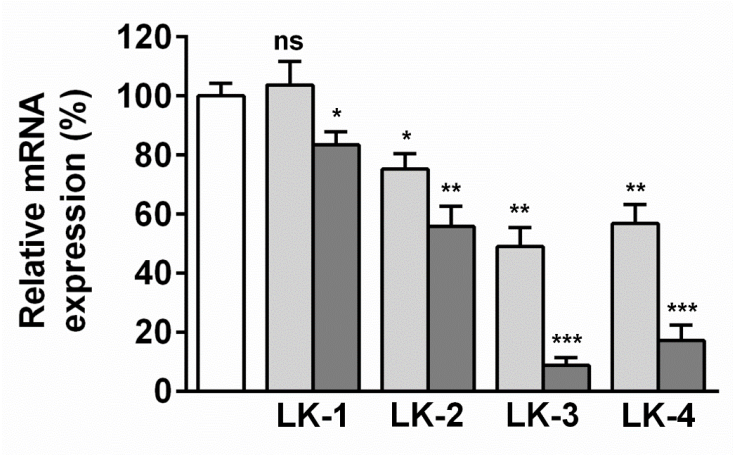

Figure 19. Inhibition of the Tat-mediated transcriptional elongation by LK peptides in HeLa cells. Relative mRNA expression of TAR-luc/TAR at 10 nM and 100 nM of each LK peptide. Control (white), 10 nM (gray), 100 nM (dark gray). Each error bar represents the standard deviation (n = 3). The markers (*), (**), (***), and (n.s.) indicate $0.01 \leq p < 0.1$, $0.001 \leq p < 0.01$, $p < 0.001$ and no significant difference compared with control, respectively.

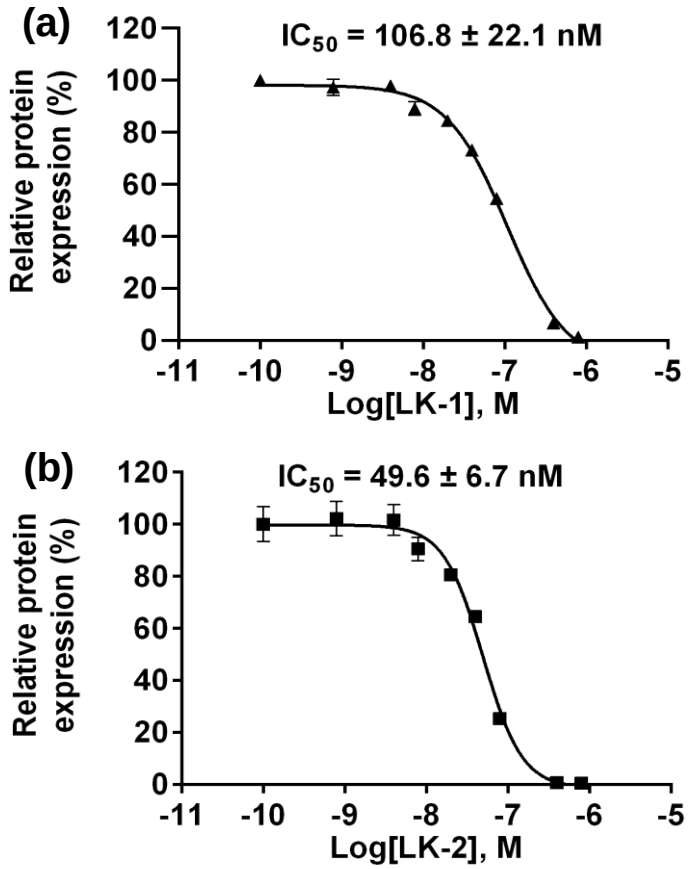

Figure 20. Inhibition of luciferase expression by (a) LK-1 and (b) LK-2 peptides in HeLa cells. Each error bar represents the standard deviation (n = 3).

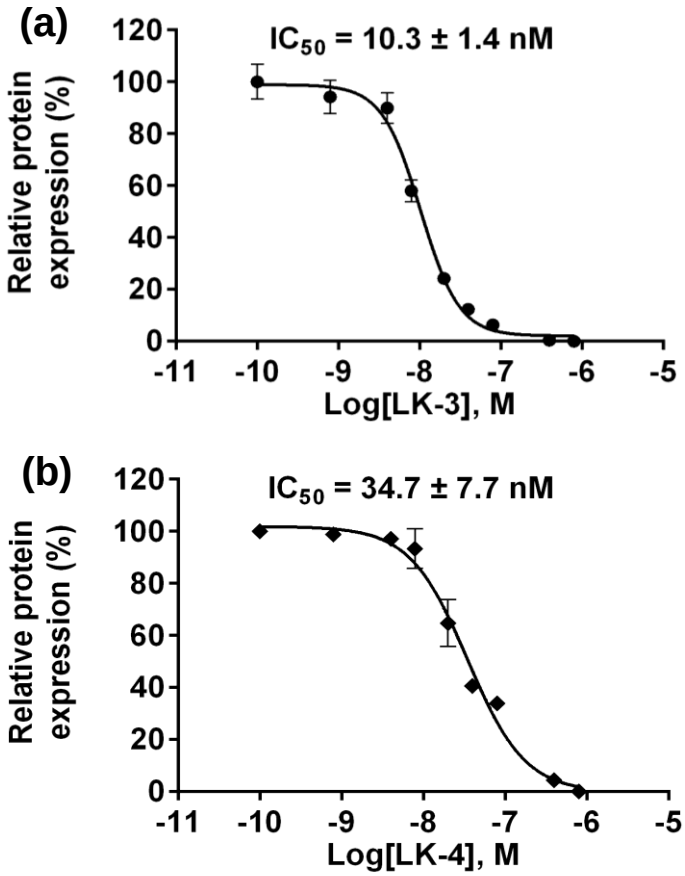

Figure 21. Inhibition of luciferase expression by (a) LK-3 and (b) LK-4 peptides in HeLa cells. Each error bar represents the standard deviation (n = 3).

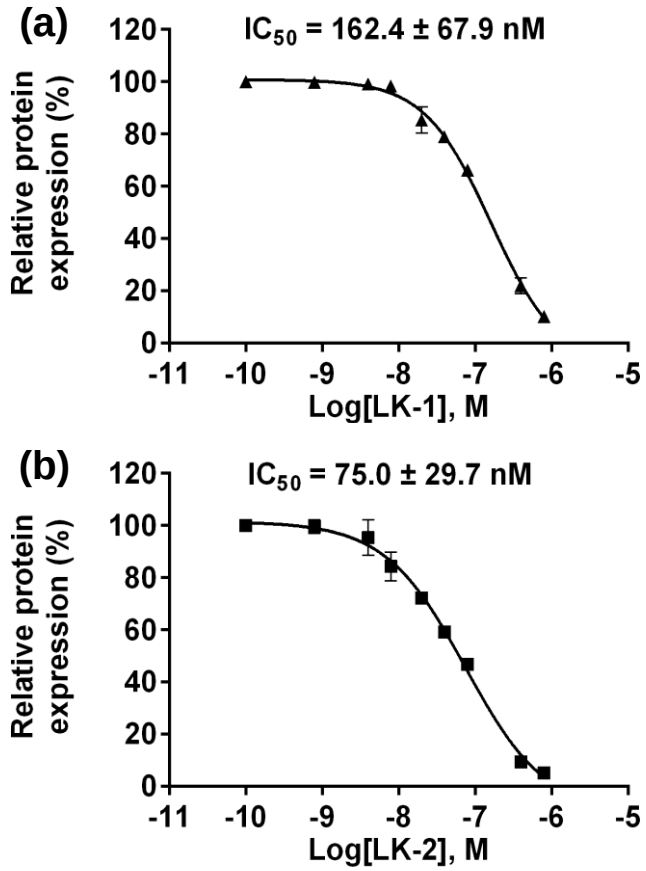

Figure 22. Inhibition of luciferase expression by (a) LK-1 and (b) LK-2 peptides in RAW 264.7 cells. Each error bar represents the standard deviation (n = 3).

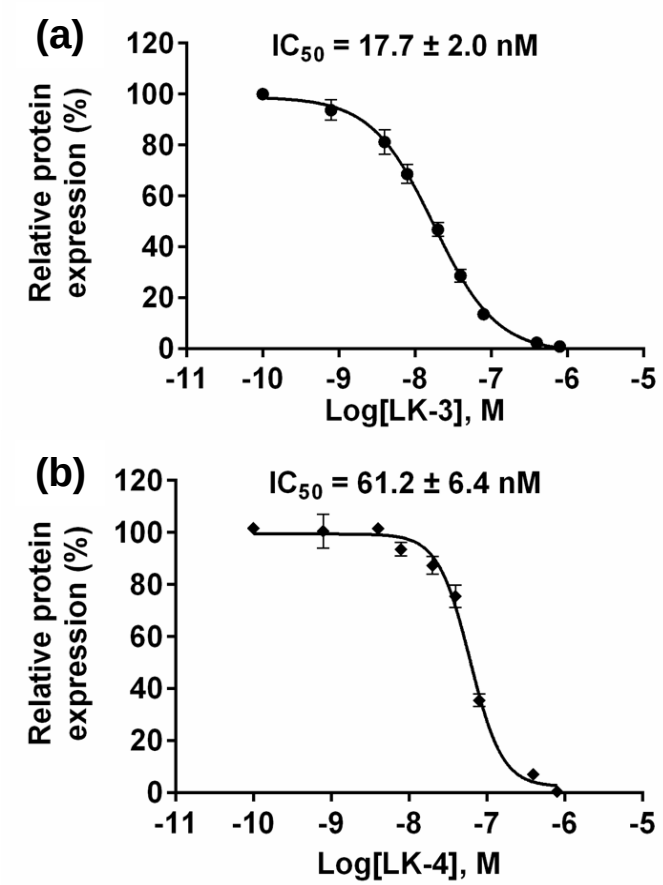

Figure 23. Inhibition of luciferase expression by (a) LK-3 and (b) LK-4 peptides in RAW 264.7 cells. Each error bar represents the standard deviation (n = 3).

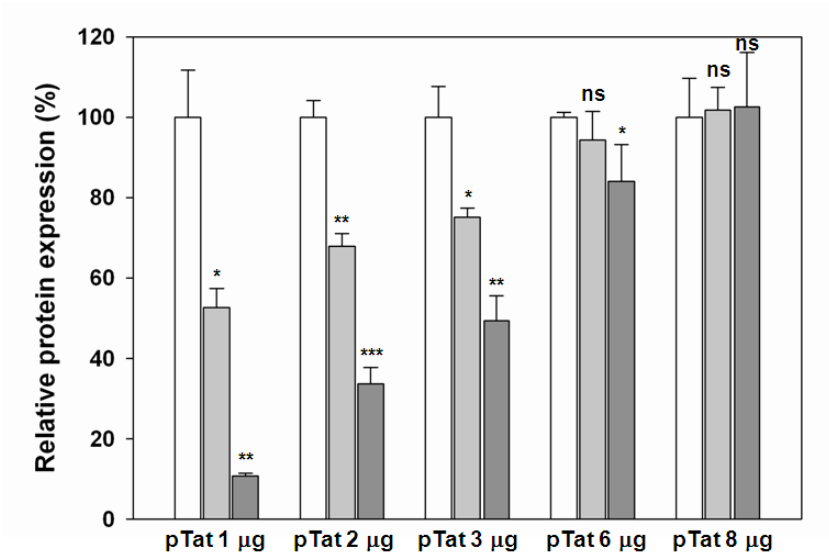

Figure 24. Inhibition of luciferase expression by LK-2 and LK-3 peptides according to pTat dose in HeLa cells. Control (white), LK-2 (gray), LK-3 (dark gray). The markers (*), (**), (***), and (ns) indicate $0.01 \leq p < 0.1$, $0.001 \leq p < 0.01$, $p < 0.001$ and no significant difference compared with control, respectively. Each error bar represents the standard deviation (n = 3).

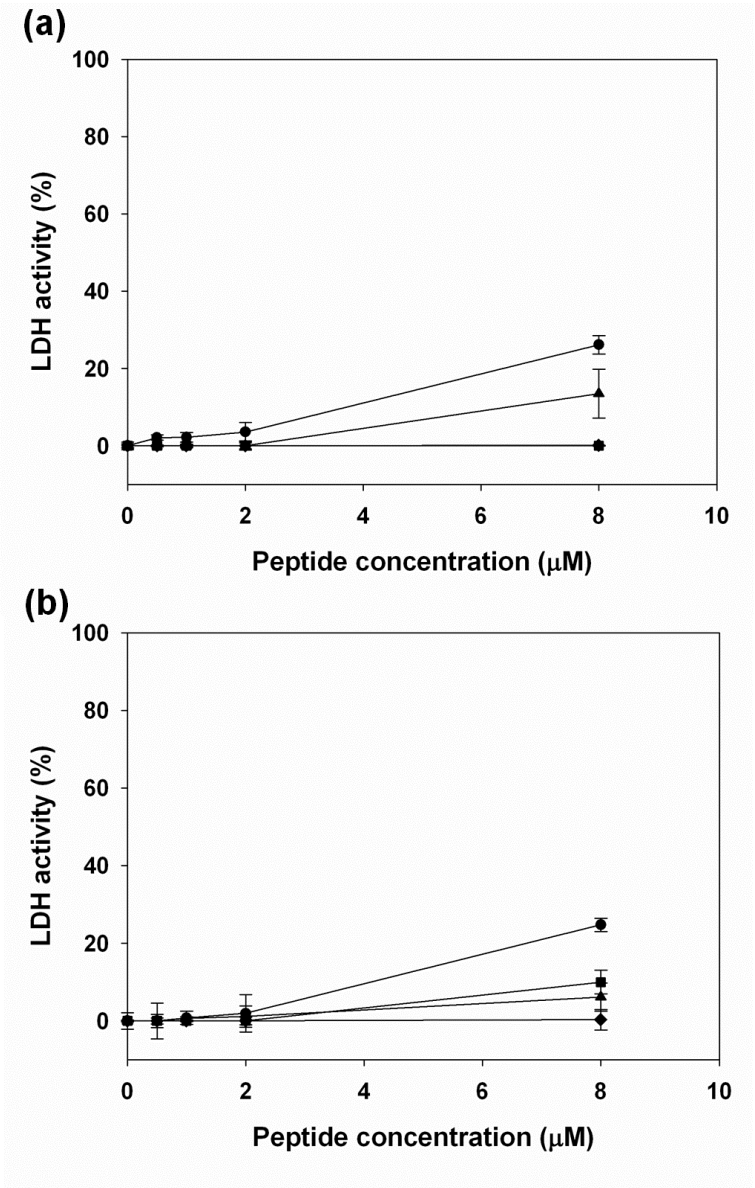

Figure 25. Relative membrane destabilization of LK-1 (▲), LK-2 (■), LK-3 (●), LK-4 (♦) in (a) HeLa cells and (b) RAW 264.7 cells. Each error bar represents the standard deviation (n = 3).

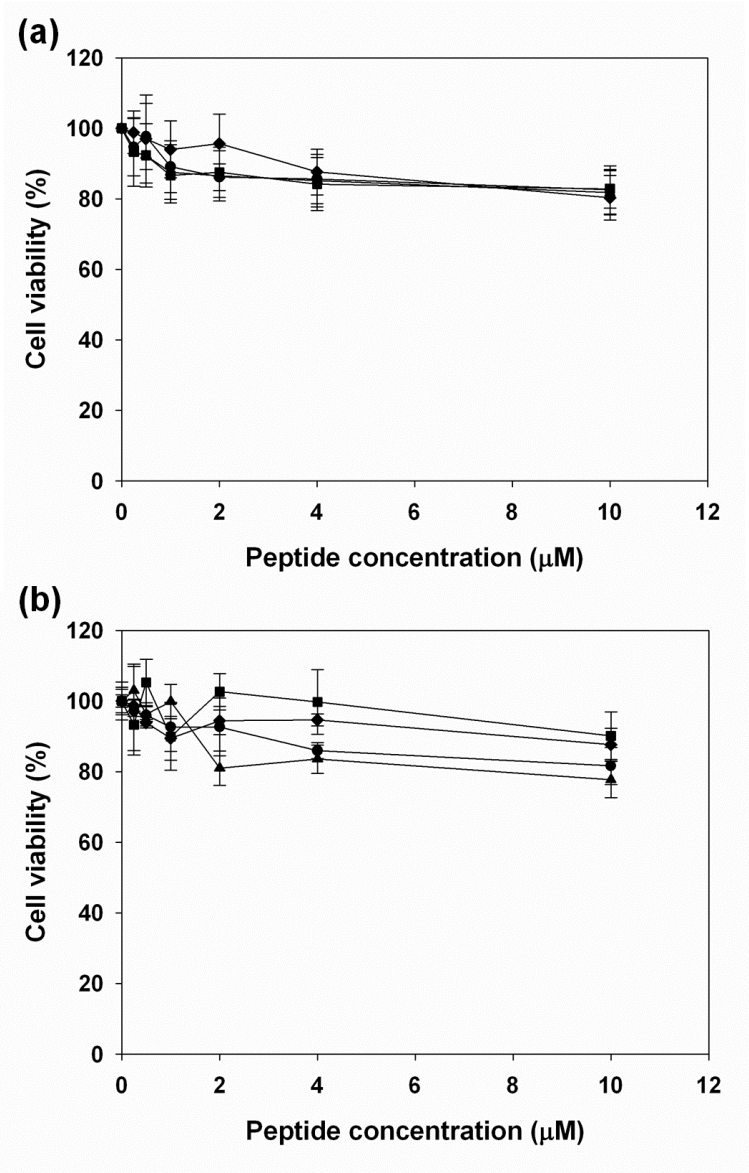

Figure 26. Relative viability of (a) HeLa cells and (b) RAW 264.7 cells after treatment with LK-1 (▲), LK-2 (■), LK-3 (●), and LK-4 (♦). Each error bar represents the standard deviation (n = 3).

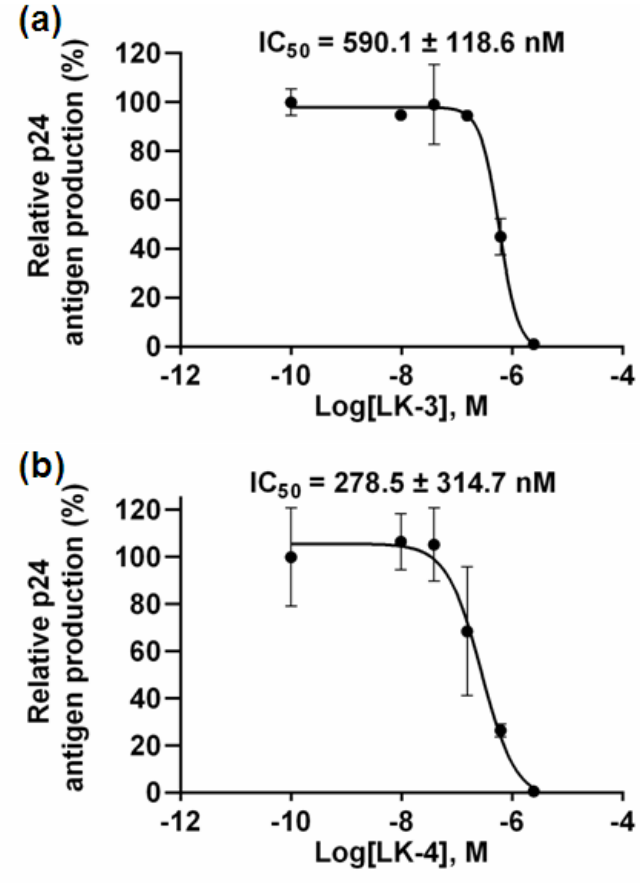

Figure 27. Inhibition of HIV-1 replication by (a) LK-3 and (b) LK-4 peptides in T-lymphoblastoid cells (MOLT-4/CCR5). Each error bar represents the standard deviation (n = 3).

Table 1. Binding affinities on TAR RNA and α-helicities of LK peptides [a]

peptide	Sequences of peptide [b]	K_d (nM)	α-helicity (%) [d]
LK-1	LKKL**L**KLLKKL**L**KLAG	63 [c]	24 /77
LK-2	LKKL**C**KLLKKL**C**KLAG	9.6 [c]	28 /77
LK-3	LKKL**C**KLLKKL**C**KLAG LKKL**C**KLLKKL**C**KLAG	0.061 [c]	91 /99
LK-4	LKKL**C**KLLKKL**C**KLAG LKKL**C**KLLKKL**C**KLAG	0.059	87 /92
R9	RRRRRRRRR	n.d [e.]	13 /15

[a] Affinities were measured at 20℃ by fluorescence anisotropy using rhodamine-Rev peptide as a probe. [b] Disulfide linkers are shown in dotted lines in LK-3. *N,N'*-1,4-Phenylenedimaleimide linkers are shown in solid lines in LK-4. N-terminal and C-terminal modification of all peptides were performed with acetylation (Ac) and amidation (NH_2), respectively. [c] Data are adopted from a previous report.[27] [d] The α-helicities of peptides were measured by circular dichroism (CD) in PBS (pH 7.4) (the first value) and in 50% TFE in the same buffer (the second value). [e] n.d.: not determined.

Table 2. Change of α-helicity [a] of LK dimers by glutathione

Peptide	α-helicity (%)	
	-GSH	+GSH
LK-3	91 /99	32 /99
LK-4	87 /92	85 /90

[a] The α-helicities of peptides were measured by circular dichroism (CD) in PBS (the first value) and in 50% TFE in the same buffer (the second value).

List of publications

A. Papers

1. Sangmok Jang, Seonju Lee, Heejin Kim, Jiyeon Ham, Ji-Hun Seo, Yeongbong Mok, Minwoo Noh, and Yan Lee*, "Preparation of pH-sensitive CaP nanoparticles with a phosphate-based block copolymer for efficient gene delivery", *Polymer* **53**, 4678-4685 (2012)

2. Jong Woo Lee, Seonju Lee, Sangmok Jang, Kyu Young Han, Younggyu Kim, Jaekyung Hyun, Seong Keun Kim*, and Yan Lee*, "Preparation of Non-Aggregated Fluorescent Nanodiamonds (FNDs) by Non-Covalent Coating with Block Copolymers and Proteins for Enhancement of Intracellular Uptake", *Molecular BioSystems* **9**, 1004-1011 (2013)

3. Minwoo Noh, Yeongbong Mok, Daichi Nakayama, Sangmok Jang, Seonju Lee, Taeho Kim, Yan Lee*, "Introduction of pH-Sensitive Upper Critical Solution Temperature (UCST) Properties into Branched Polyethylenimine", *Polymer* **54**, 5338-5344 (2013)

4. Yeongbong Mok, Daichi Nakayama, Minwoo Noh, Sangmok Jang, Taeho Kim, Yan Lee*, "Circulatory osmotic desalination by mild temperature gradient based on lower critical solution temperature (LCST) phase transition

materials", *Physical Chemistry Chemical Physics* **15**, 19510-19517 (2013)

5. Heejin Kim, Wonmin Choi, Seonju Lee, Sooyeol Kim, Jiyeon Ham, Ji-Hun Seo, Sangmok Jang, and Yan Lee*, "Synthesis of Biomembrane-Mimic Polymers with Various Phospholipid Head Groups", *Polymer* **55**, 517-524 (2014)

6. Sangmok Jang, Soonsil Hyun, Seoyeon Kim, Seonju Lee, Im-soon Lee, Masanori Baba, Yan Lee*, and Jaehoon Yu*, "Cell Penetrating, Dimeric α-Helical Peptides Are Nanomolar Inhibitors of HIV-1 Transcription", *Angewandte Chemie International Edition* (2014) (accepted)

B. Presentations

1. pH-sensitive CaP nanoparticles for efficient gene delivery, Sangmok Jang, Seonju Lee, Heejin Kim, Jiyeon Ham, and Yan Lee*, The 2nd CAMPUS Asia Symposium on Chemistry and Materials (poster presentation), March 11-13, Seoul (2013)

2. Intracellular delivery using PEG-*b*-PMOEP/CaP nanoparticles, Sangmok Jang, Jiyeon Ham, Euddeum Park, and Yan Lee*, The 8th Biomaterials Academy (poster presentation), March 29, Gwangju (2013)

3. Efficient gene delivery using pH-sensitive hybrid nanoparticles, Sangmok Jang, Seonju Lee, Jiyeon Ham, and Yan Lee*, The 112th Annual Meeting of the Korean Chemical Society (poster presentation), October 16-18, Changwon

(2013)

4. Nanomolar inhibition of HIV-1 transcription using dimeric α-helical cell-penetrating peptides, Sangmok Jang, Soonsil Hyun, Seoyeon Kim, Seonju Lee, Im-Soon Lee, Masanori Baba, Yan Lee*, and Jaehoon Yu*, The 18th Korean Peptide Protein Society Symposium (oral presentation), July 11-12, Busan (2014)

Abstract in Korean (국문 초록)

세포막을 통과하여 핵산, 펩타이드, 단백질들과 같은 생체고분자들을 전달하는 어려움은 새로운, 유력한 전달 전략들의 개발을 위한 필요성을 정당화한다. 특히, 지질과 고분자를 이용하여 세포안으로 핵산을 전달하는 현재의 비바이러스성 전략들은 제약 산업의 성공에 중대한 장벽을 나타낸다. 그러므로, 안전하고 효과적인 핵산 전달체의 개발이 빠르게 진행중이다. 칼슘인 기반 시스템이 고안할 수 있는 수많은 전달 전략들 중 한 신뢰할 수 있는 전달 시스템으로 간주한다. 그러나, 칼슘인 침전체들의 생리적 불안정성과 계속적인 성장이 생체시스템 내에서 효율적인 핵산 전달체로써의 적용을 제한한다. 이 장벽들을 극복하기 위하여, 나는 인산 기반 블록 공중합체 (PEG-*b*-PMOEP)를 합성하였고, 효율적이고 안전한 한 세포내의 유전자 전달체로써 블록 공중합체로 코팅된 칼슘인 나노파티클들을 구성하였다. PEG 블록이 칼슘인 침전체의 조절할 수 없는 성장을 막기 위하여 한 껍질을 형성하는 동안, PMOEP 블록은 칼슘인 속으로 삽입되어질 수 있다. 칼슘인 나노파티클들은 생리적 pH 7.4에서 봉입된 pDNA를 방출하지 않았으나, 엔도좀 pH 5.0에서는 인산 형태의 pH 의존적 양성자화를 통하여 pDNA를 방출하였다. PEG-*b*-PMOEP/CaP/pDNA 나노파티클들은 미래의 유전자 치료제 적용을 위한 유전자 전달체로서 큰 잠재성을 나타낸다.

한 비바이러스성 전달체로써 세포투과성 펩타이드 (CPPs)의 사용은 CPPs가 높은 세포 투과력을 성취하기 위해 필수적인 마이크로몰내의 CPPs의 농도를 필요로 한다. 그러나, 현재의 기술들은 단 시간내에 펩타이드의 불완전한 투과와 세포 내에서 마이크로몰 농도의 펩타이드의 장시간 노출 때문에 세포막 손상과 같은 다양한 부작용과 연관되어 있다. 그러므로, 나는 나노몰 농도에서 CPPs의 적용을 위해 류신과 라이신으로 이루어진 단량체 LK-1과 LK-2 뿐만 아니라 펩타이드 스테이플링 기술을 사용하여 LK-3와 LK-4로 이름지어진 이량체 알파나선형 세포투과 펩타이드를 구성하였다. 환원성의 이황화 결합 혹은 비환원성 결합을 사용한 이량화 전략은 수용액에서도 높은 알파나선형 성질을 초래하였다. 특히, 펩타이드의 알파나선형과 세포투과성 사이의 강한 관련성을 본 연구에서 관찰

하였다. 소위, 류신과 라이신으로 이루어진 LK 펩타이드들은 이전 논문에서 HIV-1의 TAR RNA에 대하여 강한 결합 친화성을 보였다. HIV-1의 TAR RNA는 바이러스성 Tat과 결합함에 의해 전사 활성화에 참여한다. LK 이량체들은 포유 세포들에서 효율적인 세포 투과와 Tat-TAR 상호작용의 저해를 위해 낮은 나노몰 수준에서 독성을 가지지 않은 채 세포막을 투과할 수 있다. T-림프아구성 세포들에서 HIV-1 복제의 효과적인 저해는 LK 이량체들, 특히 LK-3가 항바이러스성 펩타이드로서의 강한 잠재성을 지님을 제안한다.

주요어
유전자 전달, 블록 공중합체, pH-민감성, 세포 투과성 펩타이드 (CPPs), HIV-1, 펩타이드 약물, Tat-TAR 상호작용, 전사적 저해

학번: 2008-30098